Monthly Notices of the ROYAL ASTRONOMICAL SOCIETY

MNRAS **502,** 4558–4575 (2021) doi:10.1093/mnras/staa4037
Advance Access publication 2021 January 5

Probing the existence of a rich galaxy overdensity at $z = 5.2$

Rosa Calvi [1,2]★ Helmut Dannerbauer [1,2]★ Pablo Arrabal Haro [1,2] José M. Rodríguez Espinosa [1,2] Casiana Muñoz-Tuñón [1,2] Pablo G. Pérez González [3] and Stefan Geier[1,4]

[1]*Instituto de Astrofísica de Canarias, E-38205 La Laguna, Spain*
[2]*Departamento de Astrofísica, Universidad de La Laguna, E-38206 La Laguna, Spain*
[3]*Centro de Astrobíología, Departamento de Astrofísica, CSIC-IsNTA, Ctra. de Ajalvir km 4, E-28850 Torrejón de Ardoz, Madrid, Spain*
[4]*Gran Telescopio Canarias (GRANTECAN), Cuesta de San José s/n, E-38712 Breña Baja, La Palma, Spain*

Accepted 2020 December 30. Received 2020 December 29; in original form 2020 August 21

ABSTRACT

We report the results of a pilot spectroscopic program of a region at $z = 5.2$ in the GOODS-N field containing an overdensity of galaxies around the well-known submillimetre galaxy (SMG) HDF850.1. We have selected candidate cluster members from the optical 25 medium-band photometric catalogue of the project SHARDS (Survey for High-z Absorption Red and Dead Sources). 17 rest-frame ultraviolet (UV)-selected galaxies (LAEs and LBGs) with $5.15 < z_{\rm phot} < 5.27$, candidates to be physically associated with the overdensity, have been observed with the instrument OSIRIS at the GranTeCan telescope. 13 out of these 17 (76 per cent) sources have secure spectroscopic confirmations via the Lyα line at the redshift of the galaxy protocluster PCl−HDF850.1, demonstrating the high reliability of our photometric redshift method. 10 out of 13 sources are newly confirmed members. Thus, we increase the number of confirmed members in this overdensity from 13 to 23 objects. In order to fully characterize this structure we combined our data set with the sample from the literature. Beside the SMG HDF850.1, none of the 23 spectroscopically confirmed members are bright in the far-infrared/sub-mm wavelength regime ($\rm SFR_{IR}$ < few hundred $\rm M_\odot\ yr^{-1}$). The clustering analysis of the whole sample of 23 confirmed members reveals four distinct components in physical space in different evolutionary states, within $\Delta z < 0.04$ from the central region hosting SMG HDF850.1. The halo mass of the whole structure at $z = 5.2$, estimated by a variety of methods, range between 2 and $8 \times 10^{12}\ \rm M_\odot$. The comparison with literature suggests a large-scale assembly comparable to the formation of a central Virgo-like cluster at $z = 0$ with several satellite components which will possibly be incorporated in a single halo if the protocluster is the progenitor of a more massive Coma-like cluster ($> 10^{15}\ \rm M_\odot$).

Key words: galaxies: clusters: individual: PCl−HDF850.1 – galaxies: distances and redshifts – galaxies: evolution – galaxies: formation – galaxies: haloes – galaxies: high-redshift.

1 INTRODUCTION

Over the last decades, observations and theoretical predictions of galaxy clusters, the most massive gravitationally bound structures, provided very important clues on the formation and evolution of galaxies (e.g. Kravtsov & Borgani 2012). In particular, it is fairly well established that all physical processes coming into play after a galaxy has become part of a dense structure, like a group or a cluster, have a significant impact on the morphological transitions from an active (star-forming) phase to a more passive and chemical evolved phase (Andreon et al. 2004; Kauffmann et al. 2004; Baldry et al. 2006; Weinmann et al. 2006; Balogh et al. 2011). However, quantifying the impact of environment on galaxy properties, especially those closely related to the galaxy-intrinsic conditions, e.g. mass of the halo, formation time (De Lucia & Blaizot 2007; Wang, De Lucia & Weinmann 2013), is still pending.

In the last years, overdense regions at high redshifts (here after called 'galaxy protoclusters'; Overzier 2016) that evolve into galaxy clusters observed in the local Universe such as Coma or Virgo has drawn more and more attention. The observations of these regions are important not only to investigate the early stage of galaxy formation and the subsequent evolution but also to provide information on the cosmology-dependent evolving density fluctuation peaks, setting important constraints on the cosmological parameters (Kravtsov & Borgani 2012).

Many efforts have been done in recent years for finding these overdense structures at $z \sim 1.5$−2.5, the epoch when the cosmic star formation rate [(SFR) density], the accretion rate of gas feeding black holes and galaxy mergers reached their peak activity before being subsequently suppressed (e.g. Dickinson et al. 2003; Hopkins 2004; Madau & Dickinson 2014; Muldrew, Hatch & Cooke 2015; Chiang et al. 2017; Muldrew, Hatch & Cooke 2018). At these redshifts, galaxy clusters and protoclusters were in process of being transformed from dynamical overdensities to the more relaxed systems we see today. Indeed they are excellent laboratories for studying galaxy assembly and particularly the impact of environment on the galaxy populations belonging to these systems.

A variety of techniques have been established to search for galaxy overdensities such as galaxy clusters and protoclusters (galaxy clusters in formation) as the red sequence technique (e.g. Gladders & Yee 2005; Goto et al. 2008; Andreon et al. 2009; Muzzin et al.

★ E-mail: rosa.calvi@gmail.com (RC); helmut@iac.es (HD)

© 2021 The Author(s)
Published by Oxford University Press on behalf of Royal Astronomical Society

Downloaded from https://academic.oup.com/mnras/article/502/3/4558/6064312 by guest on 12 February 2026

2009; Wilson et al. 2009), the massive galaxies (e.g. Daddi et al. 2009; Gobat et al. 2011), the gaseous component in X-rays emission (e.g. Rosati, Borgani & Norman 2002; Rosati et al. 2004; Mullis et al. 2005; Stanford et al. 2006), the strong absorption in the Ly α forest (e.g. Cai et al. 2016; Miller, Bolton & Hatch 2019), the weak-lensing shear selection (e.g. Wittman et al. 2006; Gavazzi & Soucail 2007; Shan et al. 2012; Jeffrey et al. 2018), the Sunyaev–Zeldovich signatures (e.g. Staniszewski et al. 2009; Mantz et al. 2014), emission lines such as Ly α and H α through narrow-band imaging and subsequent spectroscopy (e.g. Kurk et al. 2000; Pentericci et al. 2000; Kurk et al. 2004a,b), the Lyman break features in the galaxy colour (e.g. Miley et al. 2004; Toshikawa et al. 2018), and the dust emission of star-forming galaxies (e.g. Dannerbauer et al. 2014; Planck Collaboration XXVII 2015; Greenslade et al. 2019).

Successful methods usually search for overdensities around distant, massive galaxies used as signposts such as QSOs (e.g. Djorgovski et al. 2003; Wold et al. 2003; Stiavelli et al. 2005; Kashikawa et al. 2007; Overzier et al. 2009; Stevens et al. 2010; Falder et al. 2011; Matsuda et al. 2011; Trainor & Steidel 2012; Husband et al. 2013; Morselli et al. 2014; Adams et al. 2015; Hennawi et al. 2015), high-z radio galaxies (e.g. Le Fevre et al. 1996; Pascarelle et al. 1996; Kurk et al. 2000; Pentericci et al. 2000; Venemans et al. 2004, 2005, 2007; Kajisawa et al. 2006; Hatch et al. 2011a, b; Kuiper et al. 2011; Hayashi et al. 2012; Cooke et al. 2014; Dannerbauer et al. 2014), or submillimetre galaxies (SMGs; e.g. Riechers et al. 2014; Casey et al. 2015; Casey 2016; Pavesi et al. 2018; Lacaille et al. 2019).

Especially, the search for rest-frame signatures such as the Ly α line and/or Lyman-break around possible signposts of large-scale structures had been very successful to find protoclusters from the cosmic noon to cosmic dawn. Observational evidence for indications of protoclusters were found at $z = 2.3$ and $z = 3.09$ in the field of QSOHS1700+64 and SSA22 surveys (Steidel et al. 1998, 2000, 2005) using rest-frame ultraviolet (UV) spectroscopy of a sample of candidate high-redshift galaxies selected on the basis of the Lyman break. At $z = 2.9$ and $z = 3.3$ the large spectroscopic survey VIMOS Ultra-Deep Survey (VUDS) found two exceptionally overdense region in the COSMOS field (Cucciati et al. 2014; Lemaux et al. 2014). Several structures have been also identified in the High-Redshift(Z) Emission Line Survey (Sobral et al. 2013) at three redshifts, $z = 0.8$, 1.47, and 2.23 (Cochrane et al. 2018). At higher redshift, Ouchi et al. (2005) and Jiang et al. (2018) spectroscopically confirmed luminous Ly α emission galaxy candidates tracing a massive protocluster at $z = 5.7$ in the Subaru/*XMM–Newton* Deep Field (SXDS). More recently, there are confirmations of a protocluster in the SXDS at $z = 6.5$ by using Optical System for Imaging and low-Intermediate-Resolution Integrated Spectroscopy/Gran Telescopio Canarias (OSIRIS/GTC; Calvi et al. 2019; Chanchaiworawit et al. 2019) which produces a remarkable number of ionizing continuum photons capable of ionizing a large bubble (Rodríguez Espinosa et al. 2020). This epoch is close to the full reionization of the Universe. Even though the faint primordial galaxies (being responsible for the reionization) can be difficult to observe, their location in groups or bubbles of ionized gas can enhance their visibility. Finally, Harikane et al. (2019) using Keck/DEIMOS and Gemini/GMOS spectroscopy and Castellano et al. (2018) with VLT observations found overdensities at $z = 6.6$ and $z = 7$.

When using SMGs as signposts of overdensities, the following open questions are addressed: (i) how many of these dusty starbursts – the progenitors of elliptical galaxies dominating local galaxy clusters – are members of such a structure and (ii) how much this source population contributes to the total star formation densities of individual structures. In the past years, several structures containing SMGs have been reported (e.g. Capak et al. 2011; Ivison et al. 2013; Clements et al. 2014, 2016; Dannerbauer et al. 2014; Casey et al. 2015; Hung et al. 2016; Kato et al. 2016; Lewis et al. 2018; Miller et al. 2018; Oteo et al. 2018; Pavesi et al. 2018; Harikane et al. 2019).

In Arrabal Haro et al. (2018, hereafter AH18), we presented a search for both Ly α emitters (LAEs) and Lyman Break Galaxies (LBGs) in the GOODS North field (GOODS-N). In particular, we have found 55 sources (Arrabal Haro et al. 2018) that may belong to an already known overdensity at $z \sim 5.2$ (Walter et al. 2012, hereafter W12; see Section 2 of this manuscript for details) physically related to the well-know submillimetre galaxy HDF 850.1 (e.g. Hughes et al. 1998; Dunlop et al. 2004; Walter et al. 2012; Neri et al. 2014) at $z = 5.183$. This paper presents the results of the spectroscopic follow-up of 17 candidate protocluster members through multi-object spectroscopy (MOS) with OSIRIS at the GTC. In Section 2, we discuss the sample selected from the SHARDS (Survey for High-z Absorption Red and Dead Sources) survey and in Section 3 we describe the OSIRIS MOS observations and data reduction. In Section 4, we present the results, followed by a detailed analysis in Sections 5 and 6. In Section 7, we discuss our findings in an evolutionary context. Finally, we summarize the presented work. We adopt the Lambda cold dark matter (ΛCDM) concordant Universe model ($\Omega_\Lambda = 0.7$, $\Omega_M = 0.3$, and $h = 0.7$) (Bahcall et al. 1999). Magnitudes are given in the AB system (Oke & Gunn 1983).

2 PARENT SAMPLE

Our sample is drawn from a catalogue of 1558 rest-frame UV-selected high-z galaxies presented in Arrabal Haro et al. (2018). They carried out a systematic search of LAEs and/or LBGs from $z \sim 3.35$ to $z \sim 6.8$, using 25 medium-band filters from 500 to 941 nm of the SHARDS (Pérez-González et al. 2013). This survey was conducted with OSIRIS (Cepa 2010) at the GTC, covering an area of $\sim$130 arcmin^2 in GOODS-North. Within the robust sample of 1558 sources, 528 LAEs and 1030 LBGs, 55 sources have photometric redshifts around $z = 5.2$. This spike in the redshift distribution of these rest-frame UV-selected galaxies seems to be associated with a galaxy protocluster (PCl−HDF850.1) presented by Walter et al. (2012).

Through the analysis of the environment around the well-known SMG HDF850.1, Walter et al. (2012) discovered a galaxy overdensity physically related to this dusty starburst located at $z_{CO} = 5.183$. This SMG is undetected even in deep *HST* imaging in the rest-frame UV/optical and only seen in far-infrared/submillmet wavelength regime where the spectroscopic redshifts comes from. In total, through rest-frame UV spectroscopy, Walter et al. (2012) identified additional 12 members over a narrow redshift range between $5.185 < z < 5.213$. 11 of these 13 members are recovered by our deep Ly α imaging presented in Arrabal Haro et al. (2018). Due to its faintness in the rest-frame UV/optical, no Ly α emission is expected to be seen in HDF850.1, confirmed by our data. The second source at position RA 12:36:39.8, Dec. +62:09:49.1, and redshift $z = 5.187$ is detected by SHARDS data but not selected as LAE and/or LBG.

In addition, 44 new potential members have been found. Unfortunately, beside one (QSO at $z = 5.18$; Barger et al. 2002), neither spectra nor physical information of the cluster members are published in Walter et al. (2012).

Downloaded from https://academic.oup.com/mnras/article/502/3/4558/6064312 by guest on 12 February 2026

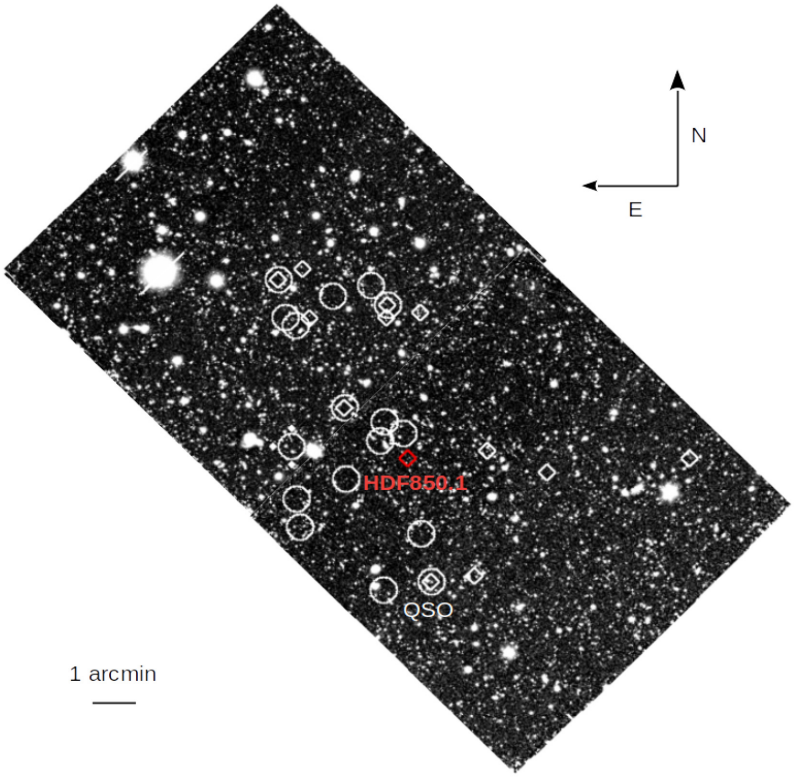


Figure 1. We show (candidate) members of the $z = 5.2$ overdensity within the SHARDS area in filter f755w17. The diamonds present the 13 members in Walter et al. (2012) including the SMG HD850.1 (red diamond). The circles present the 17 candidate members selected from AH18 for GTC OSIRIS MOS spectroscopy. Four sources have been already confirmed spectroscopically in Walter et al. (2012).

3 OBSERVATIONS

3.1 GTC OSIRIS MOS spectroscopy

The parent sample of possible overdensity members photometrically selected from Arrabal Haro et al. (2018) consists of 55 sources. We conducted a spectroscopic follow-up of a subset of candidates using the MOS capability of OSIRIS at GTC in order to confirm their physically belonging to this overdensity. The primary goal was to maximize the number of sources in a single mask. The selection of the targets was made to achieve spatial uniformity. To optimize the success rate of this pilot program, we gave higher priority to the brightest sources. The mask was filled with so-called bonus galaxies (presumably not physically related to the $z = 5.2$ overdensity) and was designed with the OSIRIS Mask Designer Tool (MD). The mask contained 24 objects, 17 LAE and LBG candidate cluster members around $z \sim 5.2$ and the seven 'bonus' sources (which are beyond the scope of this work). Furthermore, four fiducial stars, without spectral superpositions from any pair of slits, are part of the mask in order to obtain the acquisition image. The OSIRIS field of view (FoV) is a mosaic of two CCDs with a small gap in-between. In principle, the FoV in the MOS mode is 7.5 arcmin $\times$ 6.0 arcmin. We used the R2500I grism which produces a spectral resolution of $\sim$5 Å at $\lambda = 7450$ Å, with a 2 $\times$ 2 binning, so the pixels scale is 0.254 arcsec pixel^{-1}. This setup allowed us to explore the spectral range between $\sim$7330−10 000 Å. The observations (program ID: 167-GTC122/17B, PI: H. Dannerbauer) were obtained in service mode and taken at two different nights in February 2019. The number of observing blocks (OBs) were 4 and 5 during the first and second night, respectively. Each OB consisted of two frames of 1368 s each. The pure observing time was 6.9 h with a seeing of 0.7–1.0 arcsec. The first night was dark and the second night was grey time. Only in the first night the conditions were photometric. The 2 arcsec aperture circular holes were used for the fiducial stars and thus, for centring the mask with high precision. The science object slits have a slit length of 20 arcsec and a width of 1.2 arcsec. As the objects are very faint, we decided not to do dithering, thus avoiding to add extra noise to the data. The standard star used for flux calibration is Feige 66. In Fig. 1, we show the locations of the 17 targets and the previously known 13 protocluster members from W12 around the SMG HDF850.1.

3.2 Data reduction

The individual CCD images were reduced and combined using IRAF routines (Tody 1986). The data consist of the scientific and calibration images. We subtracted the bias and normalized the flat for each OBs separately. We used a reference flat for each chip to remove detector and geometrical distortions. Then, the slits frames were aligned and then combined to obtain the master image to improve the S/N and remove the cosmic rays. Considering the low signal-to-noise (S/N) and complex nature of the observed spectra, we decided to analyse separately the frames of the first and second night. Only after the extraction of the individual spectra, they were combined to maximize the S/N. We separated the individual 24 slits, 9 in Chip1 and 15 in Chip2 and we trimmed off the edges in the science frames before aligning the spectra and performing the wavelength calibration. We performed the spectroscopic calibration using IRAF routines on the individual slit frames. Every slit is also contaminated by the emission spectrum of the Earth's atmosphere, thus we used the OH sky

Downloaded from https://academic.oup.com/mnras/article/502/3/4558/6064312 by guest on 12 February 2026

emission lines for the wavelength calibration of the spectra.[1] Using the IRAF-NOAO package, we identified the corresponding wavelength sky emission lines within our slit frames. Fourth-order Chebyshev polynomials were fit along the spatial direction to provide a smooth master sky model to subtract it from the 2D spectrum. The sky subtraction process near emission lines can be problematic; therefore, we also looked for significant peaks in the one-dimensional spectra which show an asymmetric line profile. We extracted a 1D spectrum by summing the flux along a window of 6 pixels (∼1.5 arcsec). The size of the extraction window allowed us to optimize the flux counts of each emission line. Then, we find the centroid of the signal in the spectrum and we consider a window of 6 pixels around this centroid which contains the signal (+3 pixels on the right, −3 pixels on the left), we extract the spectrum's lines in this window and, using IRAF tasks, we check for the presence of an asymmetric profile. So, the total flux is the sum along the *x*-axis of this extracted spectrum. We focused on the 1D and 2D visual inspection in the wavelength range of 7300−7800 Å. Those spectra with a clear continuum break and/or emission line indicating a precise redshift were denoted as grade A, secure detection. On the opposite, if from visual inspection we are not able to obtain a clear detection, we performed a second iteration of the sky subtraction to look for a significant peak in the 2D spectrum. Sources detected in this way are grade B, tentative detection. A non-detection is category C. These are objects for which the resulting spectra have very low S/N. During this process we found that not all science frames were useful. This was caused by non-photometric conditions of the second night, which was taken in grey and not in dark time. For this reason we discarded all the 10 science frames of the second night in which we could not even detect the brightest sources. In the end, we used a total of 8 science frames to obtain the highest S/N 2D spectra for our observed targets.

The spectra were flux calibrated using the spectroscopic standard star Feige 66 observed during the same observing run/night. The spectroscopic standard was used to determine the response curve of the spectrograph, and in turn was used to flux-calibrate the spectra of our targets. First, we reduced and calibrated in wavelength the spectroscopic standard star in the same manner as the science frames. However, since the standard star was taken with a wider slit width (2.5 arcsec), we used single slit flats for the standard from the OSIRIS webpage.[2] Then, we extracted the 1D spectrum of the standard star using the task IRAF/APALL. Knowing the exposure time and the extinction correction, we matched the 1D spectrum of the spectroscopic standard in units of ADU s^{-1} to the available flux density catalogue of Oke (1990), tabulated in the *onedstds* directory of IRAF. Thus, we obtained the flux transformation from ADU s^{-1} to erg s^{-1} cm^{-2} $Å^{-1}$ to calibrate the science frames. The typical accuracy of the obtained spectroscopic redshifts is to the third digit.

4 RESULTS

4.1 Spectroscopic redshifts

In total, we obtained spectroscopic redshifts for 13 out of 17 candidate protocluster members via the Ly α line. All 13 sources are physically associated with the protocluster. The spectra of the 13 cluster members, 10 with very good S/N (grade A) plus 3 additional sources with reasonably good S/N (grade B) are shown in Figs 2 and 3, respectively. The success rate of detections – 13 out of 17 with spectroscopic redshift – is 76 per cent. These sources show reliable line detection in the 2D spectra and signs of an asymmetric profile in the 1D spectra, resulting in reliable spectroscopic redshifts. The object IDs, coordinates, magnitudes, SHARDS photometric redshifts, obtained spectroscopic redshifts, source types (LAE or LBG), and quality flags (grades) are listed in Table 1. The redshifts have been measured at the peak of the Ly α emission line simply using $z_{\rm spec} = \frac{\lambda_{\rm obs}}{1216\,Å} - 1$. Several studies have demonstrated that most high-redshift galaxies have sufficiently high SFRs to drive galactic scale winds. Signatures of the wind can then be seen both in the shape of Ly α line profile itself and in the redwards velocity offset of the Ly α line of few hundreds of km s^{-1} with respect to the systemic redshift caused by the transit through the IGM's thick optical depth (Shapley et al. 2003; Steidel et al. 2010; Hashimoto et al. 2015, 2019). However, the aim of this paper is not to probe the kinematic state of the interstellar medium (ISM) in these galaxies but to probe the existence of an overdensity at the redshift close to the SMG's one. Thus, the offset in velocity values does not affect the association with the SMG and we assume that the peak marks the centre of the line.

The spectroscopic redshift of these 13 sources ranges from $5.155 \leq z \leq 5.224$ ($\Delta z < 0.069$). We compare the spectroscopic redshifts of these 13 confirmed members with the photometric redshifts derived from the SHARDS data (Arrabal Haro et al. 2018), see Fig. 4. The resulting residuals $\delta_z = |z_{\rm phot} - z_{\rm spec}|$ range between $0.002 \leq \delta_z \leq 0.055$, with $\bar{\delta_z} = 0.026$, in close agreement with the 1:1 relation between these two redshift measures. This analysis shows the very high reliability of the photometric redshifts derived by Arrabal Haro et al. (2018), indispensable for the success of our spectroscopic observations.

We observed four sources from Walter et al. (2012) to verify the reliability of our spectroscopic measurements. Three of them have been successfully recovered. Our measured spectroscopic redshifts are consistent with those from W12 (see Table 1 within the given uncertainties, accurate to the third digit for both samples). The failure of the non-detected source, an LBG galaxy with $m_{\rm AB} > 26.92$ at the SHARDS filter f755*w*17, can be well explained by its very faint magnitude, more than ∼0.5 mag above the faintest sources with spectroscopic redshifts. The fact that some of our sources have been spectroscopically detected previously (Barger et al. 2002; Walter et al. 2012) gives credibility to the spectra we have obtained. To summarize, our spectroscopic observations have increased the number of member galaxies, by 10 new confirmed members, from 13 to 23.

A stacked spectrum was done by cutting all the confirmed spectra in a window of 100 pixels around the lambda-emission position, used as reference point and then summing up all frames obtained. The stacked spectrum is shown in Fig. 5. It exhibits enhanced S/N as compared to the individual galaxy spectra. The asymmetry of the stacked line is noticeable. If the sky lines were contaminating the stacked spectrum we would expect a more symmetric line. Therefore, we have very high confidence in the 13 (both grade A and B) spectroscopically confirmed candidates that we have detected.

4.2 Flux and equivalent width measurements

We measured the Ly α fluxes and rest-frame equivalent widths (EW_0) manually, using IRAF, from the Ly α emission lines in the spectra,

[1] We used the LRIS catalogue of sky emission lines between 6400 and 10 500 Å from http://www.astrossp.unam.mx/resast/standards/NightSky/skylines.html.
[2] http://www.gtc.iac.es/instruments/osiris/

Downloaded from https://academic.oup.com/mnras/article/502/3/4558/6064312 by guest on 12 February 2026

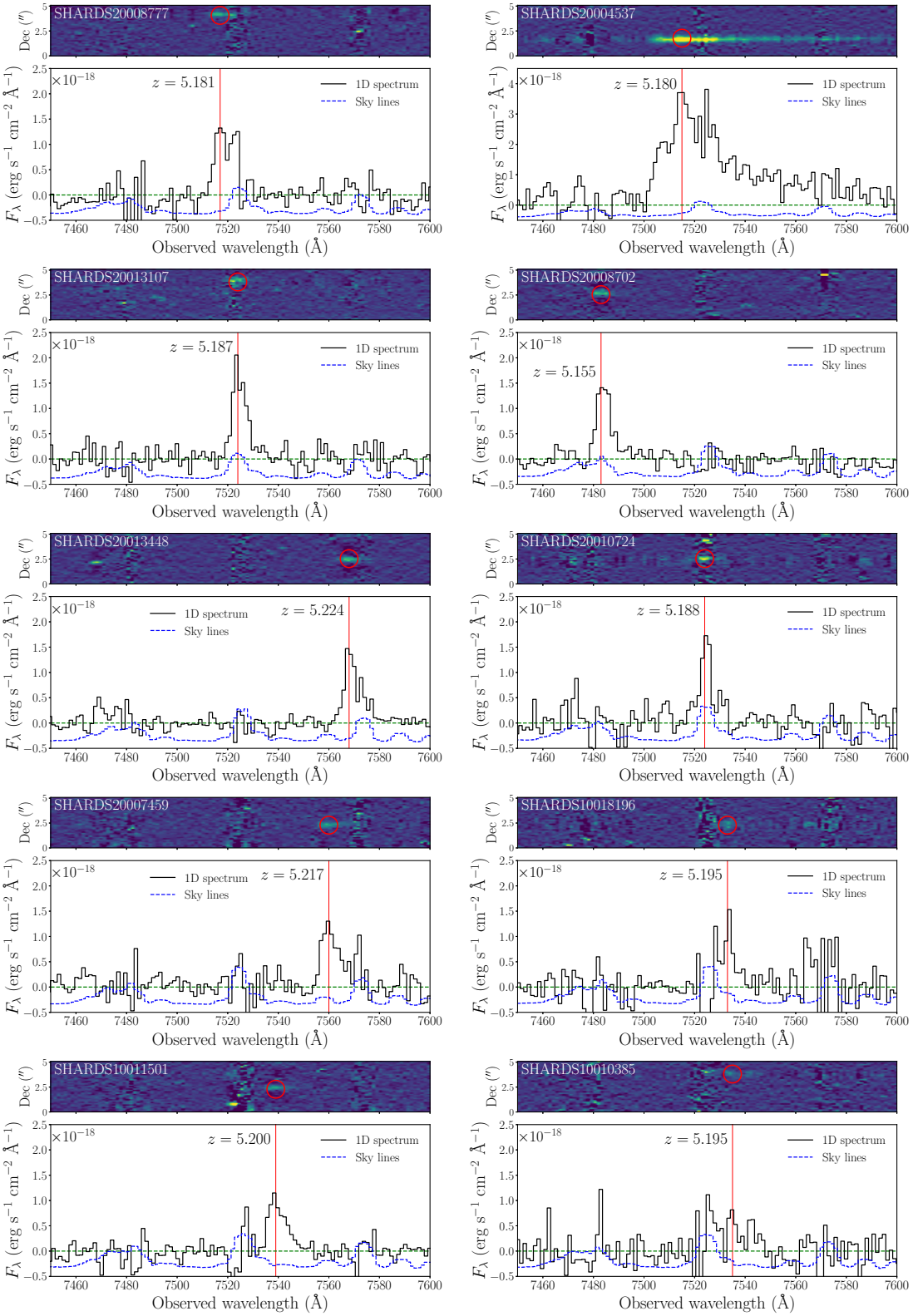


Figure 2. 2D and 1D spectra of the sources classified like secure detection, grade A in Table 1. The black lines are the collapsed one-dimensional spectra. The solid red line shows the peak of the Ly α emission line, with the corresponding redshift written besides. The blue spectra are the sky lines spectra scaled down so they do not interfere with the actual spectra of the sources. The horizontal green dashed line shows the zero flux level.

Downloaded from https://academic.oup.com/mnras/article/502/3/4558/6064312 by guest on 12 February 2026

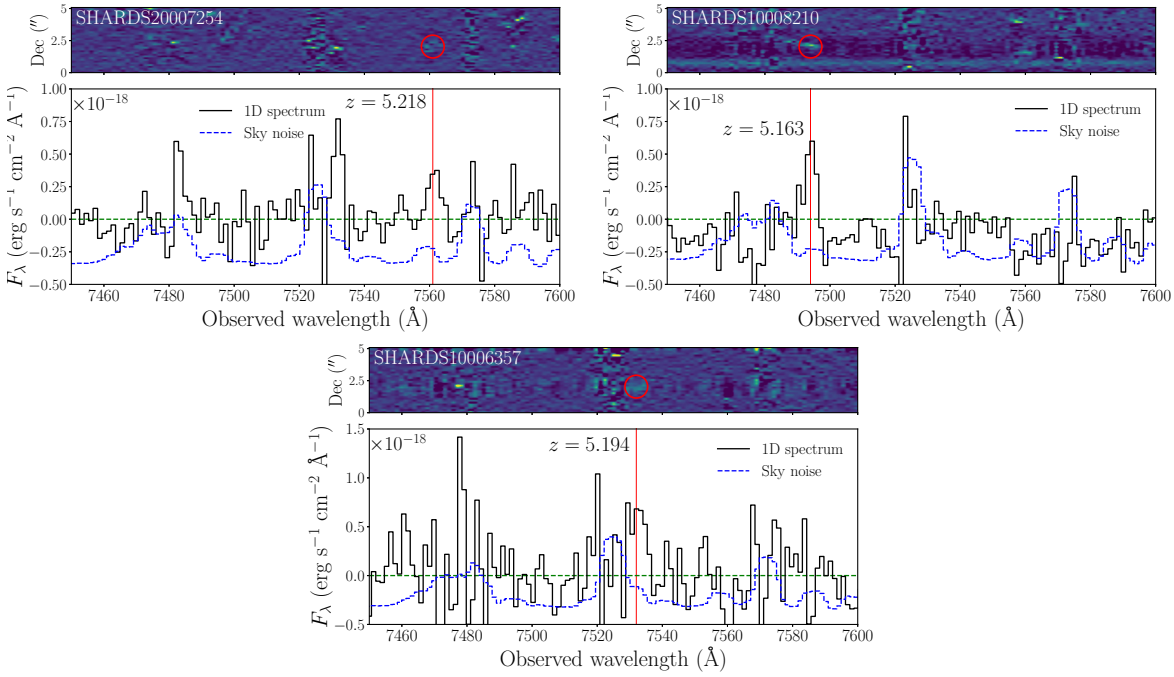


Figure 3. 2D and 1D spectra of the sources classified like tentative detections, i.e. grade B in Table 1. The meanings of all lines are the same as in Fig. 2.

Table 1. Observed targets.

Source	RA (J2000.0)	Dec. (J2000.0)	m_{AB}	z_{phot}	z_{spec}	Type	Grade observations	Previous
(1)	(2)	(3)	(4)	(5)	(6)	(7)	(8)	(9)
$z = 5.2$ protocluster candidate members								
SHARDS10005737	12:37:13.38	62:12:39.2	25.77 ± 0.25	5.26	–	LBG	C	
SHARDS10006357	12:37:15.63	62:16:23.6	25.75 ± 0.18	5.19	5.194	LAE	B	5.189 (W12)
SHARDS10008210	12:37:14.50	62:15:32.4	26.11 ± 0.26	5.18	5.163	LBG	B	
SHARDS10008850	12:36:55.39	62:15:48.8	>26.92	5.15	–	LBG	C	5.190 (W12)
SHARDS10010385	12:36:58.43	62:16:15.0	25.68 ± 0.16	5.16	5.195	LAE	A	
SHARDS10011501	12:37:05.52	62:16:01.3	25.50 ± 0.08	5.17	5.200	LAE	A	
SHARDS10018196	12:37:12.48	62:15:21.1	25.48 ± 0.14	5.17	5.195	LAE	A	
SHARDS20004537	12:36:47.96	62:09:41.4	22.74 ± 0.01	5.19	5.180	LAE	A	5.18, 5.186 (B02; W12)
SHARDS20007254	12:37:12.80	62:11:32.0	26.07 ± 0.34	5.22	5.218	LBG	B	
SHARDS20007459	12:37:03.31	62:13:31.5	$25.45 \pm 0,24$	5.27	5.217	LBG	A	5.213 (W12)
SHARDS20008702	12:37:12.08	62:10:54.1	25.11 ± 0.11	5.21	5.155	LAE	A	
SHARDS20008777	12:36:56.70	62:09:30.5	25.03 ± 0.14	5.19	5.181	LAE	A	
SHARDS20008932	12:36:57.29	62:12:49.4	25.16 ± 0.11	5.23	–	LAE	C	
SHARDS20010724	12:36:56.51	62:13:13.6	25.25 ± 0.39	5.23	5.188	LAE	A	
SHARDS20011455	12:36:53.09	62:12:59.5	25.42 ± 0.15	5.23	–	LAE	C	
SHARDS20013107	12:36:49.79	62:10:45.0	25.22 ± 0.12	5.21	5.187	LAE	A	
SHARDS20013448	12:37:03.61	62:11:58.5	24.48 ± 0.11	5.22	5.224	LAE	A	

Notes. Column (1) SHARDS source name. Column (2) J2000.0 right ascension of the targets. Units of right ascension are hours, minutes, and seconds. Column (3) J2000.0 declination of targets. Units of declination are degrees, arcminutes, and arcseconds. Column (4) The magnitudes are given in the AB system (Oke & Gunn 1983). The magnitudes are measured in the SHARDS filter *f*755*w*17. Column (5) Photometric redshift measured from the photometry published in AH18, the typical error is ±0.07. Column (6) Spectroscopic redshift, the typical error is accurate to the third digit. Column (7) Object type (LAE or LBG). Column (8) Quality of line detection, grade A is secure detection, B tentative detection, and C no detection. Column (9) *z*-spec known in the literature.

see Table 2. This method guarantees a high degree of accuracy. Using the IRAF/SCOPY and IMSUM tasks, we located the position of the centroid of each emission line along the slit. Then, we defined an extraction window as ±3 pix along the *x*-axis from the centroid. The total flux of a source is the sum along the six-contiguous spatial rows of this extracted spectrum. Then, using IRAF/SPLOT we marked two continuum points before and after the line. To determine the noise, we repeated the measurements five times for each source. The fluxes and the EW_0 for the 13 sources classified as A and B are shown in Table 2. As some sources are localized on top of sky lines, the errors in these cases were computed by adding to both the EW_0 and flux measurement errors of 25 per cent of the mean value, a conservative approach. The values of EW_0 range between 75 and 188 Å. The exception is the QSO whose EW_0 is above 300 Å. The high values of EW_0 are not unusual to find in a protocluster (see e.g. Steidel et al. (2000), Dey et al. (2016)). This indicates more efficient

Downloaded from https://academic.oup.com/mnras/article/502/3/4558/6064312 by guest on 12 February 2026

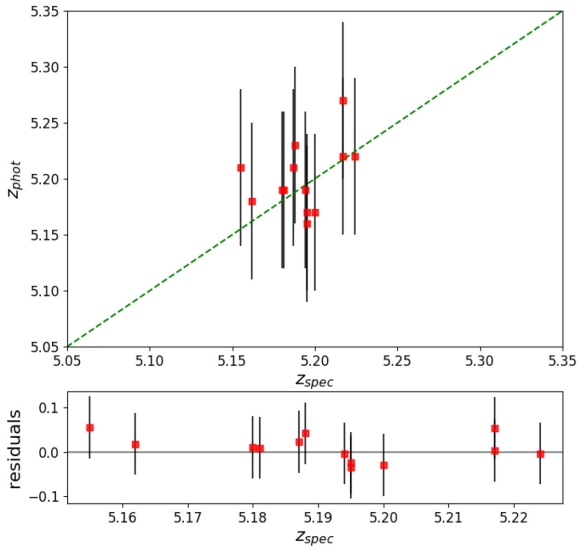


Figure 4. Comparison between the photometric and spectroscopic redshifts of the 13 LAEs/LBGs classified with grades A and B. The green dashed line is the 1:1 relation. In the bottom panel, we show the residuals. This analysis shows that the photometric redshifts derived from the SHARDS data set in GOODS-N in Arrabal Haro et al. (2018) are very accurate and thus very reliable for the search of overdensities.

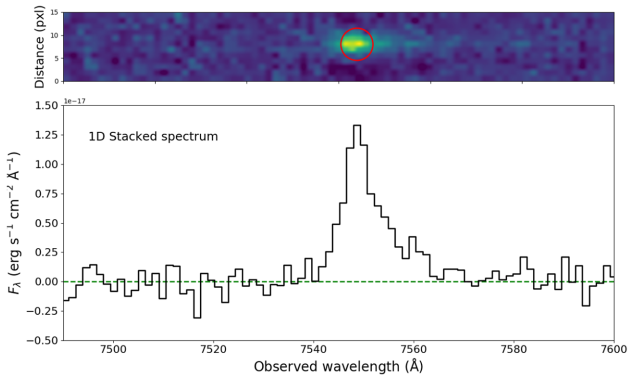


Figure 5. The stacked 2D and 1D spectrum of the 13 confirmed overdensity members at z=5.2 with reliable detections.

ionization and more extreme ionizing conditions of the nebular gas which are conducive to the escape of ionizing photons (Tang et al. 2019). In all cases beside one, the EW_0s obtained from the spectra are (much) larger than those derived from the SHARDS medium-band filters (Arrabal Haro et al. 2018, given in parenthesis in Table 2 of this work). This may indicate that only with spectroscopy a reliable EW could be determined.[3] Using evolutionary synthesis models, Otí-Floranes & Mas-Hesse (2010) show that once the equilibrium phase has been reached, the intrinsic Ly α equivalent widths should never be above ∼100 Å. Almost all our sources lie above this theoretical limit. Except for the QSO, our values of EW_0 are lower than the critical limit of Ly α rest-frame equivalent width of 240 Å obtainable from ionization by a massive star population (Charlot & Fall 1993).

[3]For example, the case that the Ly α line falls outside the plateau of the filter response could be responsible that photometric measurements underestimate the EW.

These values are only consistent with very young (age $< 10^7$ yr), almost coeval star formation episodes.

4.3 Star formation rates

To compute the SFRs, we follow the standard Kennicutt calibration (Kennicutt 1998), assuming Case B recombination and a Salpeter initial mass function with a mass range of 0.1–100 $M_\odot$, considering a $\frac{F_{Ly\alpha}}{F_{H\alpha}}$ flux ratio of 8.7 (Brocklehurst 1971; Dopita & Sutherland 2003). The following conversion from luminosity to SFR is assumed:

$$\frac{\mathrm{SFR(H}\,\alpha)}{\mathrm{M}_\odot\ \mathrm{yr}^{-1}} = \frac{7.9\times10^{-42}}{8.7}\,\frac{L_{\mathrm{Ly}\alpha,\mathrm{obs}}}{\mathrm{erg\ s}^{-1}}, \quad (1)$$

where $L_{\mathrm{Ly}\,\alpha,\mathrm{obs}}$ is the observed luminosity computed as

$$L_{\mathrm{Ly}\alpha,\mathrm{obs}} = 4\pi\,(d_\mathrm{L})^2\,F_{\mathrm{Ly}\alpha} \quad (2)$$

and d_L is the luminosity distance calculated at each redshift. This method follows a traditional and straightforward way of computing SFRs. However, it should be noted that it is based on the assumption of a star formation episode producing stars at a constant rate during tens of Myr, until the birth and death of the most massive ionizing stars reach equilibrium. The SFRs for each source are directly derived from the observed Ly α luminosity. No attempts were made to correct for internal extinction as we do not have the possibility to determine the extinction for each object. None the less, the (expected) extinction of LAEs at $z \sim 5.2$ is not large, in general below $A_\mathrm{V} = 1$ (e.g. Ouchi et al. 2009; Bouwens et al. 2015; Arrabal Haro et al. 2018).

5 CHARACTERIZATION OF THE $z = 5.2$ OVERDENSITY

In this section, we discuss the properties of this protocluster at $z = 5.2$. To carry out our analysis, we will use all members spectroscopically confirmed by our work and the work by Walter et al. (2012). Thirteen sources come from our work and 10 from W12. We should note that three sources from W12 have been confirmed through our spectroscopic campaign and we use our measurements for the subsequent analysis. We list all the members and their properties in Table 3.

5.1 Radio and far-infrared properties

None of the 23 spectroscopially confirmed members (including HDF850.1) have a radio counterpart down to ∼11 μJy (5σ) in the extremely deep JVLA 1.4 GHz map of GOODS-N presented by (Owen 2018). This detection limit equals an SFR of ∼1500–2000 $M_\odot$ yr^{-1}, significantly higher than the SFRs derived for our sources from the Ly α line ranging between ∼0.3 and 3 $M_\odot$ yr^{-1} (see Table 2), and in the range of typical high-z dusty starbursts. We note that this structure would not have been found through the radio selection technique using the 1.4 GHz band to search for galaxy clusters in formation in the distant Universe (Daddi et al. 2017). Furthermore, we searched the photometric public catalogue of 3306 'super-deblended' dusty galaxies obtained by Liu et al. (2018) in GOODS-N. HDF850.1 seems to be marginally detected in the 1.4 GHz at $S_{1.4\,\mathrm{GHz}} \sim 11$ μJy (Liu et al. 2018; Owen 2018).[4] Beside HDF850.1, none of the cluster members are bright in the far-infrared/(sub)mm wavelength regime. In addition, no other

[4]The flux is not reported in any solid detection list up to now.

Downloaded from https://academic.oup.com/mnras/article/502/3/4558/6064312 by guest on 12 February 2026

Table 2. Spectroscopically confirmed protocluster members in this work.

Source	z_{spec}	$Flux_{Ly\,\alpha}$ ($erg\,s^{-1}\,cm^{-2}$) ($\times 10^{-18}$)	$L_{Ly\,\alpha}$ ($erg\,s^{-1}$) ($\times 10^{42}$)	$SFR_{Ly\,\alpha}$ ($M_\odot\,yr^{-1}$)	EW_0 (Å)
(1)	(2)	(3)	(4)	(5)	(6)
SHARDS20008777	5.181	7.9 ± 0.3	2.23 ± 0.08	2.02 ± 0.08	163 ± 28 (110)
SHARDS20004537	5.180	41.6 ± 1.8	11.7 ± 0.5	10.6 ± 0.45	315 ± 70 (35)
SHARDS20013107	5.187	13.1 ± 0.2	3.70 ± 0.06	3.36 ± 0.05	155 ± 61 (60)
SHARDS20008702	5.155	10.4 ± 3.0	2.91 ± 0.84	2.64 ± 0.76	149 ± 61 (97)
SHARDS20007254	5.218	2.4 ± 0.1	0.70 ± 0.03	0.63 ± 0.03	120 ± 25
SHARDS20013448	5.224	9.1 ± 2.3	2.62 ± 0.66	2.38 ± 0.60	188 ± 71 (89)
SHARDS20010724	5.188	9.7 ± 3.0	2.75 ± 0.85	2.50 ± 0.77	142 ± 50 (111)
SHARDS20007459	5.217	9.4 ± 0.4	2.70 ± 0.11	2.45 ± 0.10	166 ± 16
SHARDS10018196	5.195	5.5 ± 0.5	1.56 ± 0.14	1.42 ± 0.13	75 ± 29 (78)
SHARDS10008210	5.163	1.2 ± 0.2	0.33 ± 0.05	0.30 ± 0.05	92 ± 13
SHARDS10011501	5.200	8.4 ± 0.1	2.40 ± 0.01	2.18 ± 0.01	156 ± 18 (134)
SHARDS10010385	5.195	4.1 ± 0.5	1.16 ± 0.14	1.05 ± 0.13	118 ± 20 (26)
SHARDS10006357	5.194	5.5 ± 0.7	1.56 ± 0.20	1.42 ± 0.18	129 ± 52 (9)

Notes. Column (1) SHARDS source name. Column (2) Spectroscopic redshift. Column (3) Ly α flux. Column (4) Ly α luminosity. Column (5) SFR from Ly α. Column (6) Rest-frame Ly α equivalent width. In parenthesis, we give the equivalent width previously measured from the SHARDS medium-band filters (Arrabal Haro et al. 2018).

significant molecular gas reservoir was revealed in this field at the redshift of HDF850.1 (Riechers et al. 2020).

Beyond $z = 5$ only a few systems with SMGs being the signpost of an galaxy overdensity confirmed through spectroscopy are known in the literature. One is the overdensity consisting of three LBGs physically related to the SMG AzTEC-3 (Riechers et al. 2010; Capak et al. 2011; Riechers et al. 2014; Pavesi et al. 2018) and the other a pair of the dusty starburst galaxy CRLE at $z = 5.667$ and the 'normal' main-sequence galaxy HZ10 at $z = 5.654$ (Pavesi et al. 2018). In addition, photometric data indicate that both systems could be part of a larger galaxy overdensity. In the case of the dusty starburst FLS3 at $z = 6.3$ (Riechers et al. 2013), an LBG overdensity cannot be completely excluded (Laporte et al. 2015). To summarize, up to now no system – dusty starburst surrounded by rest-frame UV bright galaxies – is known with such a high number of spectroscopically identified members. The extent of our system at the sky is about 10 arcmin × 10 arcmin, respectively, in physically scales about 4 × 4 Mpc, consistent with size predictions by Muldrew et al. (2015) and Casey (2016). HDF850.1 has an SFR of ∼850 $M_\odot\,yr^{-1}$ (W12). Whereas the sum of all 12 members (without the QSO) observed by us sum up to maximal ∼40 $M_\odot\,yr^{-1}$. Even applying an extinction correction the SFR of this protocluster is strongly dominated by the SMG. Within 1 arcmin, we find three other rest-frame UV bright galaxies. To summarize, we infer that the dusty starburst HDF850.1 could evolve into the brightest cluster galaxy (BCG) and thus should be the centre of this overdensity.

5.2 Clustering analysis

In the standard ΛCDM model, the small haloes form first, then merge to form larger ones. One model that may provide insights into the gravitational collapse of dark matter haloes (DMH) is the spherical top-hat collapse model (Gunn & Gott 1972; Gunn 1977; Peebles & White 1981). This model assumes a highly idealized halo, with no interactions with the surrounding matter, characterized by its large overdensity Δ with respect to the background density. As the collapse starts, the overdensity Δ increases drastically and it is predicted to be $\Delta_c \sim 178$ times denser than the background. Δ_c indicates the critical density of a virialized halo. Some simulations suggest that this occurs at $\Delta_c \sim 200$, more or less independent of cosmology, and so a common mass estimator is M_{200} which is approximately the virial mass if $\Omega_M = 1$ (White 2001).

According to *N*-body simulations the larger the scale the less the virialization (Jang-Condell & Hernquist 2001; Hetznecker & Burkert 2006; Davis & Natarajan 2010; Davis, D'Aloisio & Natarajan 2011). With this in mind, the term 'virialized' is not properly correct for high-redshift protoclusters. Such structures typically are aligned along a filamentary structure and their members are unlikely to be governed by the virial theorem. However, even if the concept of virialization is not the same referred to the massive bound DMHs by $z = 0$, it is important to understand whether the distribution in both position and velocity space of our sources is consistent with the existence of any collapsing process at this redshift. In the following, we explore the spatial and velocity structures, the possibility of a 'core' (virialized or currently virializing) and the existence of other substructures.

5.3 Spatial and velocity fields

The spectroscopic observations presented in this work confirmed 13 LAEs and LBGs (three of them from Walter et al. 2012) belonging to the overdensity at redshift $z = 5.2$. For a complete analysis we decided to include the 10 sources from Walter et al. (2012), having in total 23 sources physically related to the overdensity, including the dusty starburst HDF850.1. The redshift distribution of all 23 cluster members is shown in Fig 6. The overall covered redshift is $5.155 \leq z \leq 5.224$ ($\Delta z = 0.07$). This range corresponds to a comoving radial distance of 34.8 Mpc (i.e. a angular size distance of ∼5.6 Mpc). Assuming that the SMG lies at the centre of the overdensity, the plot of contours of the objects surface density in Fig. 7 illustrates that the protocluster lies predominantly in an elongated filamentary structure around the SMG along north-east to south-west direction. A density enhancement is located on the NE side while about half of the galaxies lie in regions that are underdense compared to that in NE suggesting that they are approaching the SMG from other directions along the filament. The histogram of redshift shows an evident peak at $z_{peak} \sim 5.19$ and two adjacent peaks. The

Downloaded from https://academic.oup.com/mnras/article/502/3/4558/6064312 by guest on 12 February 2026

Table 3. All sample of the spectroscopically confirmed protocluster members.

Cluster member	Source name	RA J2000.0	Dec. J2000.0	z_{spec}	$M_\star$ (10^9 $M_\odot$)	z-range	Region clump*	Reference	Comments
(1)	(2)	(3)	(4)	(5)	(6)	(7)	(8)	(9)	(10)
PCl−HDF850.1 − 01		12:36:00.0	62:12:26.1	5.199	1.32 ± 0.73	$5.180 \leq z \leq 5.208$	4	W12	
PCl−HDF850.1 − 02		12:36:26.5	62:12:07.4	5.200	2.39 ± 1.11	$5.180 \leq z \leq 5.208$	4	W12	
PCl−HDF850.1 − 03		12:36:37.5	62:12:36.0	5.185	1.52 ± 0.94	$5.180 \leq z \leq 5.208$	CR	W12	
PCl−HDF850.1 − 04		12:36:39.8	62:09:49.1	5.187		$5.180 \leq z \leq 5.208$	2	W12	
PCl−HDF850.1 − 05	SHARDS20004537	12:36:47.96	62:09:41.4	5.180	6.70 ± 0.33	$5.180 \leq z \leq 5.208$	2	This work (B02, W12)	QSO
PCl−HDF850.1 − 06		12:36:49.2	62:15:38.6	5.189	5.83 ± 1.22	$5.180 \leq z \leq 5.208$	1	W12	
PCl−HDF850.1 − 07	SHARDS20013107	12:36:49.79	62:10:45.0	5.187	28.10 ± 4.61	$5.180 \leq z \leq 5.208$	2	This work	
PCl−HDF850.1 − 08		12:36:52.0	62:12:25.8	5.183		$5.180 \leq z \leq 5.208$	CR	W12	HDF850.1
PCl−HDF850.1 − 09		12:36:55.4	62:15:48.8	5.190	1.43 ± 0.76	$5.180 \leq z \leq 5.208$	1	W12	
PCl−HDF850.1 − 10		12:36:55.5	62:15:32.8	5.191	3.74 ± 1.98	$5.180 \leq z \leq 5.208$	1	W12	
PCl−HDF850.1 − 11	SHARDS20010724	12:36:56.51	62:13:13.6	5.188	6.43 ± 4.39	$5.180 \leq z \leq 5.208$	CR	This work	
PCl−HDF850.1 − 12	SHARDS20008777	12:36:56.70	62:09:30.5	5.181	0.19 ± 0.12	$5.180 \leq z \leq 5.208$	2	This work	
PCl−HDF850.1 − 13	SHARDS10010385	12:36:58.43	62:16:15.0	5.195	1.97 ± 1.16	$5.180 \leq z \leq 5.208$	1	This work	
PCl−HDF850.1 − 14	SHARDS20007459	12:37:03.31	62:13:31.5	5.217	2.03 ± 0.60	$5.217 \leq z \leq 5.224$	3	This work (W12)	
PCl−HDF850.1 − 15	SHARDS20013448	12:37:03.61	62:11:58.5	5.224	2.00 ± 1.09	$5.217 \leq z \leq 5.224$	3	This work	
PCl−HDF850.1 − 16	SHARDS10011501	12:37:05.52	62:16:01.3	5.200	0.21 ± 0.14	$5.180 \leq z \leq 5.208$	1	This work	
PCl−HDF850.1 − 17		12:37:09.9	62:15:31.1	5.191	1.19 ± 0.75	$5.180 \leq z \leq 5.208$	1	W12	
PCl−HDF850.1 − 18		12:37:11.1	62:16:38.6	5.208	10.20 ± 2.02	$5.217 \leq z \leq 5.224$	1	W12	
PCl−HDF850.1 − 19	SHARDS10018196	12:37:12.48	62:15:21.1	5.195	0.25 ± 0.80	$5.180 \leq z \leq 5.208$	1	This work	
PCl−HDF850.1 − 20	SHARDS20008702	12:37:12.08	62:10:54.1	5.155	0.54 ± 0.37	$5.155 \leq z \leq 5.163$	-	This work	
PCl−HDF850.1 − 21	SHARDS20007254	12:37:12.80	62:11:32.0	5.218	4.86 ± 1.48	$5.217 \leq z \leq 5.224$	3	This work	
PCl−HDF850.1 − 22	SHARDS10008210	12:37:14.50	62:15:32.4	5.163	7.07 ± 4.02	$5.155 \leq z \leq 5.163$	1	This work	
PCl−HDF850.1 − 23	SHARDS10006357	12:37:15.63	62:16:23.6	5.194	3.29 ± 1.15	$5.180 \leq z \leq 5.208$	1	This work (W12)	

Notes. Column (1) Protocluster ID. Column (2) SHARDS source name. Column (3) J2000.0 right ascension of the targets. Column (4) J2000.0 declination of the targets. Column (5) Spectroscopic redshift. Column (6) Stellar masses. Column (7) Redshift range of the galaxy. Column (8) Proto-groups (CR indicates the central region). Column (9) Redshift reference. Column (10) Additional comments.

Downloaded from https://academic.oup.com/mnras/article/502/3/4558/6064312 by guest on 12 February 2026

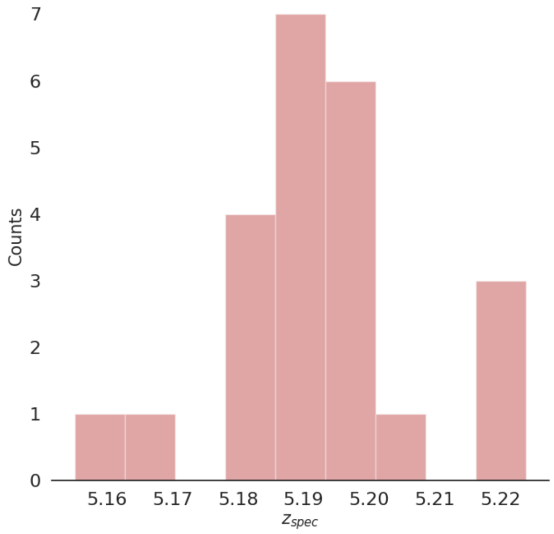


Figure 6. Redshift distribution of the 23 objects used in the Friends-of-Friends algorithm. For the protocluster galaxies in common with W12, we adopted our redshift determinations. Redshift bins are 0.01.

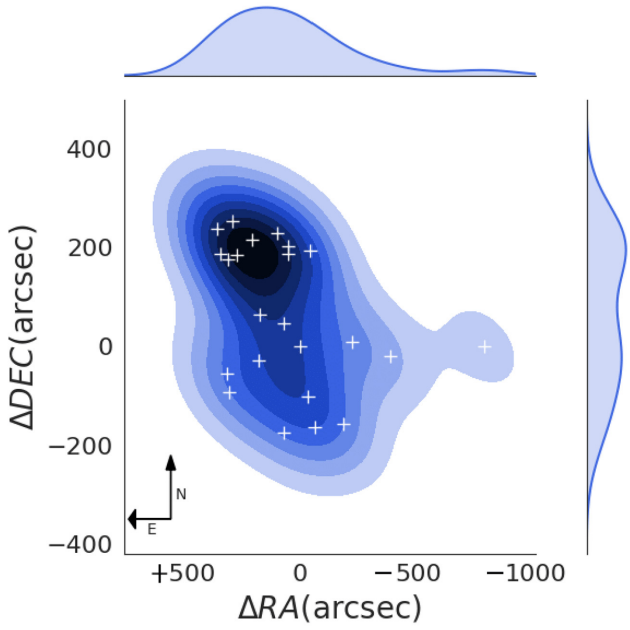


Figure 7. Using kernel density estimation, we show the contour density plot in relative coordinates (offsets in RA and Dec.). The origin (RA, Dec.) = (0,0) is defined as the position of the SMG HDF850.1. The white crosses are the positions of the 23 sources. The marginal charts show the distribution of the two variables.

central bin includes 18 galaxies which range between $5.180 \leq z \leq 5.208$ ($\Delta z = 0.028$,$\Delta v_{\rm los} \sim 1360\,{\rm km\,s^{-1}}$), the lower bin includes two galaxies with redshift $z = 5.155$ and $z = 5.163$ ($\Delta z = 0.008$, $\Delta v_{\rm los} \sim 390\,{\rm km\,s^{-1}}$), and finally, three galaxies lie within the higher bin $5.217 \leq z \leq 5.224$ ($\Delta z = 0.007$, $\Delta v_{\rm los} \sim 340\,{\rm km\,s^{-1}}$). The sources lying at the near edge of the redshift range (selected by our medium-band filter) could be 'contaminants' (close to protocluster but not members of it) as well. However, we decide to keep these sources in the subsequent analysis because they could be part of a filamentary structure falling into the potential of the central high-density region. As shown in Fig. 7, we identify two main regions: the NE region and the South region. In the NE region, we find a concentration of ten galaxies with redshifts higher than the SMG, nine within the central redshift bin (5.189−5.208) and one within the low-redshift bin (5.163) which has an ambiguous spectroscopic redshift and could be an interloping galaxies that is not a true member. The remaining galaxies are more widespread around the SMG (in the centre of the plane) lying in a region stretching from SW to SE. Their redshifts fall within a broad range that includes all the three redshift bins (5.155−5.224), suggesting that they are associated with the protocluster but belong to physically distinct structures.

5.4 Statistical properties in terms of stellar masses

The stellar masses for the sources are estimated using the CIGALE code (Code Investigating Galaxies Emission; Burgarella, Buat & Iglesias-Páramo 2005; Noll et al. 2009; Boquien et al. 2019). This code has been developed to study the evolution of galaxies by comparing modelled galaxy spectral energy distributions (SEDs) to observed ones. We refer to Arrabal Haro et al. (2020) for details on the use of CIGALE to fit SEDs on the sample of 1558 high-z LAEs and LBGs selected from the SHARDS galaxies in the range $3.4 < z < 6.8$. We provide the stellar masses for 21 out of 23 members which are part of our LAE/LBG sample. In case of HDF850.1 (#8) and the galaxy (#4), no stellar masses can be provided (the latter one is not part of our sample). Stellar mass estimates are shown in Table 3. These values lie in the range $(0.018-2.81) \times 10^{10}\,{\rm M_\odot}$ with a median $M_\star$ of $(2.03 \pm 1.67) \times 10^9\,{\rm M_\odot}$. In Fig. 8, we show the three-dimensional distribution of all 23 galaxies according with their stellar masses (indicated with different sizes) and redshifts (indicated with the colour bar). We include the galaxies #8 and #4, for which we do not have the stellar mass estimates, considering for them the highest value of $M_\star$ in our list. It is clear that the LAEs/LBGs fall into several possible velocity groupings along the line of sight (*los*). A number of galaxies with redder colours (lying a higher redshift than HDF850.1) and low-intermediate masses are grouped on one side (NE) of the SMG galaxy. This concentration of galaxies in the NE region, already seen in the density plot in Fig. 7, could be an indication of a population of 'proto-red sequence' galaxies. The presence of a passive sequence, similar to that in low-redshift clusters, has been both demonstrated in observations in protocluster at $z \sim 2-3$ (Diener et al. 2013; Cucciati et al. 2014; Lemaux et al. 2014; Strazzullo et al. 2016; Wang et al. 2016) and predicted in simulations (Contini et al. 2016). Indeed, the *red sequence method* is a powerful tool for finding clusters by looking for overdensities of galaxies that form a red sequence (Kurk et al. ; Kodama et al. 2007; Zirm et al. 2008). Several galaxies with violet-blues colours appear located on the opposite side of the SMG. Additionally, there is a number of galaxies a bit further respect to the SMG that might represent a filamentary distribution within the overdensity.

From a statistical analysis of the stellar masses, we try to understand if the galaxies in the NE region could be the sign of a more evolved population of more massive galaxies. In Fig. 9, we plot the cumulative distribution functions of the stellar masses in the two main regions in which the protocluster is separated. Most of the galaxies, ∼70–80 per cent, range from 10^9 to $10^{10}\,{\rm M_\odot}$ while only 20 per cent have a stellar mass less than $10^8\,{\rm M_\odot}$ regardless of their location in the protocluster. Using a two-sample KS test, we also investigate whether the mass measurements of galaxies in NE and South regions are consistent with being drawn from an incomplete but uniformly

Downloaded from https://academic.oup.com/mnras/article/502/3/4558/6064312 by guest on 12 February 2026

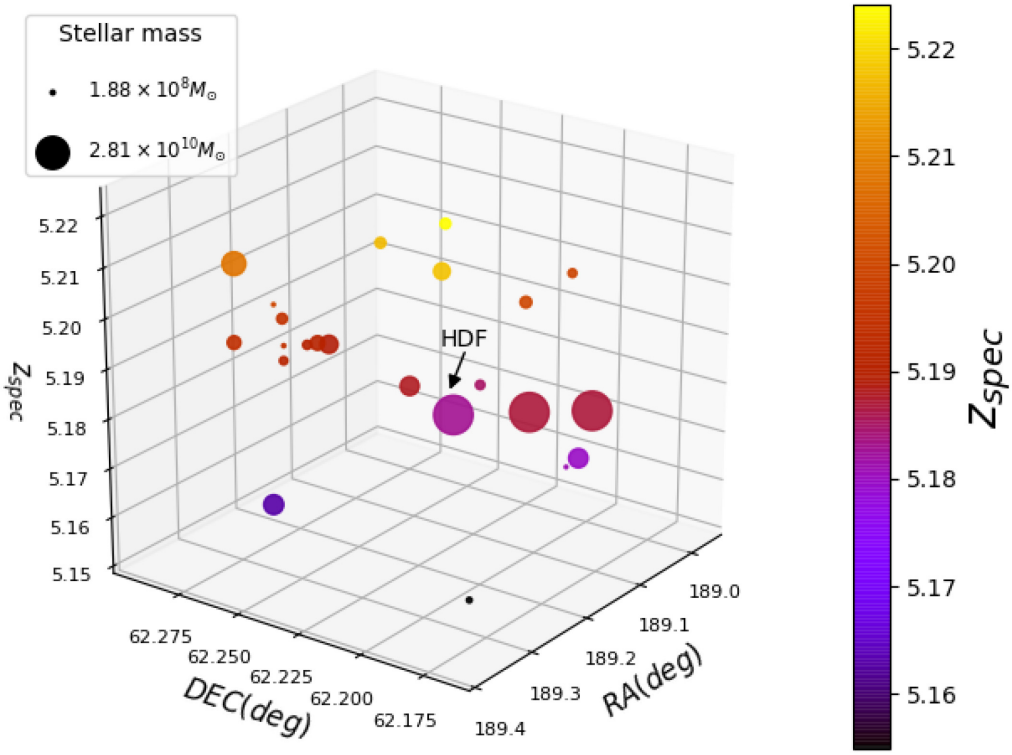


Figure 8. Three-dimensional plot of the distribution of galaxies in right ascension (x-axis), declination (y-axis), and redshift (z-axis). The circle size indicates the different stellar masses in the range $1.88 \times 10^8\,\mathrm{M}_\odot < M_\star < 2.81 \times 10^{10}\,\mathrm{M}_\odot$. The colour bar indicates the spectroscopic redshift.

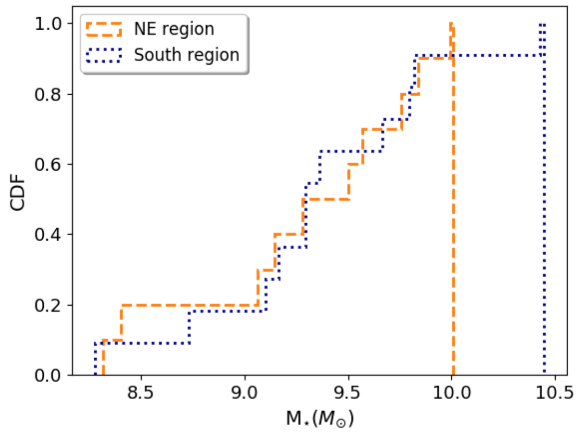


Figure 9. Cumulative distribution function of the stellar masses in the NE region (orange dashed line) and in the South region (dotted blue line).

distributed sample on the FoV. We find a p value of 99.9 per cent, thus we cannot reject the hypothesis that the distributions of the two samples are the same. Finally, we do not find any strong evidence of an enhancement of the stellar mass density in the NE side, compared to the South one where galaxies are more dispersed, but we cannot avoid to note the peculiarity of this substructure. Indeed, the galaxies in the NE region appear to be assembled faster with a star formation activity still on-going.

5.5 Evidence of substructures

To assess the existence of any grouping or clustering which can characterize underlying substructures in the density field of our protocluster we use a Friends-of-Friends (FoF) algorithm which follows the method developed both to search for groups and clusters in a magnitude-limited survey (Huchra & Geller 1982; Eke et al. 2004; Berlind et al. 2006) and in cosmological simulations (Einasto et al. 1984; Davis et al. 1985; Lacey & Cole 1994; Jenkins et al. 2001; Gottlöber & Yepes 2007). This algorithm select groups which correspond as closely as possible to real 3D groups, at least in a statistical sense. An iterative procedure is applied, according to which two galaxies belong to the same system if their projected separation and their *los* velocity dispersion are less than a fixed threshold. It should be noted that the shifting of the Lyα line centre due to the photon strong resonant scattering from neutral hydrogen in the ISM, produces large uncertainties in the measurement of the velocity dispersions. However, when estimating the overdensity structure, we assume an isotropic velocity distribution in 3D space and the differences in redshift are caused by their *los* component velocities within the redshift space. With this assumption the component σ_{los} of the velocity dispersion is $\frac{\sigma}{\sqrt{(3)}}$.

We first adopt as linking parameters a projected mutual distance $D_{\mathrm{L}} = 0.5$ Mpc, that is almost two times the radius R_{200} of a group, and a *los* velocity dispersion, V_{L}, fixed at 500 km s^{-1} rest frame to avoid the interlopers. We chose these linking lengths to explore the systems within the protocluster that already constitute a real interacting group. For each galaxy we searched for its first neighbour and, by a recursive procedure, we added neighbours of neighbours until no more were found. We identify in the NE region two gravitationally bounded systems: a group of three galaxies and another of six galaxies. We

Downloaded from https://academic.oup.com/mnras/article/502/3/4558/6064312 by guest on 12 February 2026

define these systems as 'trial' group. To study the internal dynamics of the two systems in the NE region with $N_{\rm gal} \geq 3$ (from now on group-I and group-II) and eventually asses the presence of a 'core' in the protocluster, we required a more accurate membership determination. Indeed, the accidental inclusion of interlopers is one of the major problems in identifying groups in redshift space. For these two groups we used the well-defined statistical approach by Beers, Flynn & Gebhardt (1990) and we computed the position of the geometrical centre in each group and the gapper. The Gapper algorithm is a robust statistical estimator recommended over the canonical rms standard deviation as this algorithm is insensitive to outliers and thus reproduces more accurately the true dispersion of the systems with sizes <10 (Beers et al. 1990). The velocity dispersion is given by

$$\sigma_{\rm gapper} = \frac{\sqrt{(n)}}{n(n-1)} \sum_{i=1}^{n-1} w_i g_i, \tag{3}$$

where $w_i = i(n-i)$ and $g_i = x_{i+1} - x_i$ is the velocity dispersion. Then, we restricted the membership to galaxies within $\pm\sigma_{los}$ from the median group redshift and located within a projected distance of $\pm R_{200}$ from the geometrical centre. Assuming that these systems are collapsing (approximately virialized), R_{200} is an approximation of the radius which defines a sphere with the mean interior density 200 times the mean matter density at that epoch ($\langle\rho\rangle(1+z)^3$). To obtain an estimate of the radius R_{200}, we follow the same procedure as Chanchaiworawit et al. (2019). We assume an NFW halo model (Navarro, Frenk & White 1996, 1997) and with a given σ_{los}, the radius R_{200} is expressed as

$$R_{200} = 3\sigma_{\rm los} \left(\frac{1}{560\pi\, G(1+z)^3\langle\rho\rangle} \right)^{\frac{1}{2}}, \tag{4}$$

where G is $4.9 \times 10^{-9} ({\rm km\,s^{-1}})^2\,{\rm Mpc^{-1}\,M_\odot}$. We iterated the process till when the last two iterations have identical output. We find that only a pair of galaxies in the group-I are bound within $R_{200} = 104$ kpc. The pair of galaxies in the group−I have spectroscopic redshifts of 5.19 and 5.191 and a relative velocity of 300 km s^{-1}. From the value of R_{200} we computed the associated dynamical masses M_{200} using the equation (9),

$$\frac{3M_{200}}{4\pi R_{200}^3} = 200\langle\rho\rangle(1+z)^3. \tag{5}$$

The derived mass is $M_{200} \sim 9.4 \times 10^{12}\,{\rm M_\odot}$. The high-mass estimate can be explained as a natural bias because clumps in high-density regions collapse earlier and accrete faster their mass. These values are rare but not impossible to find at $z > 5$ (e.g. Chanchaiworawit et al. 2019). In any case, under the assumption of virialization and spherical symmetry for the system, this mass has to be considered an upper limit.

These results confirm a segregation of galaxies in the protocluster. A more evolved halo is located in the densest NE region. All galaxies in this region range within a projected distance of <670 kpc and a probable case of an 'off-centre' core is present. A pair-like structures are also found by (Toshikawa et al. 2014; Topping, Shapley & Steidel 2016; Toshikawa et al. 2020). These authors suggests that large-scale galaxy/group assembly start by $z \geq 4$ with primordial satellite components that appear in parallel with the formation of central protoclusters. The NE region might be considered as the very massive halo, where galaxies are dynamically bound and are falling into the potential of the central high-density region. We define the NE region as the 'clump1' of the overdensity.

An analysis of the velocity distribution of the southern sources have shown that a fraction of the galaxies have relative low velocities even if they still did not enter in a common halo. Thus, they can be part of dynamically young systems in the process of merging. With this purpose, we investigated these galaxies by considering different and increasing values of $D_{\rm L}$ (550–600–700–800 kpc) and we run again the FoF. We identify four substructures. The first is located in the central part of the overdensity structure. It hosts the SMG that is separated by <500 kpc in physical distance from the closer galaxies and their relative $\sigma_{los} \sim 300$ km s^{-1}. Since the SMG should be the proto-BCG of the overdensity, we find that its formation history is possibly the result of multiple high-z progenitors which could assemble into a single BCG at low-z, in agreement with simulations (Ragone-Figueroa et al. 2018). We define it as 'central region'. The small group of three galaxies associated with the QSO CXOHDFNJ123647.9+620941 (Barger et al. 2002, 2003) reside on the periphery of the structure. They have a physical distance from the centroid of the group within ∼300 kpc and a velocity dispersion $\sigma_{los} = 281$ km s^{-1}. We define it as 'clump2'. Another substructure in the SE region is made up by three galaxies – in the highest redshift bin $5.217 \leq z \leq 5.224$ – with a physical distance within ∼250 kpc from the centre of the group and $\sigma_{los} = 400$ km s^{-1}. We name it 'clump3'. Finally, two galaxies on the SW side with a physical distance within ∼100 kpc and $\sigma_{los} \sim 50$ km s^{-1} are defined as 'clump4'. The galaxies in the last two groups appear clustered in redshift as well as spatially. However, their small number cannot allow us to draw any definitive conclusions. They can be attributed to some filaments along the *los*, providing further evidence that the structure is dynamically young.

The separation between the central region and the mean redshift of the four clumps is within $\Delta z < 0.04$ and is equal to 484 kpc, 170 kpc, 2.75 Mpc, and 1.2 Mpc in physical scale, for clump1, clump2, clump3, and clump4, respectively. We show these clumps in the 2D plot in Fig. 10. The sky distribution in the 3D and in the 2D plot evidences the presence of a few galaxies that do not belong to any substructure. They are probably located at the outskirts, suggesting the existence of a larger filamentary structure.

5.6 Phase-space diagram

In an attempt to further understand the dynamical state of this overdensity we complete our analysis showing in Fig. 11 the position of the confirmed members in the phase-space diagram (e.g. Oman, Hudson & Behroozi 2013; Haines et al. 2015; Jaffé et al. 2015). This diagnostic was developed for virialized NFW haloes (including assumptions about spatial symmetrical distribution) which generally is not the case for any galaxy protocluster. However, although all these assumptions for such sparse structures, composed of several independent infalling groups, might not be entirely correct, some authors (e.g. Shimakawa et al. 2014) have made estimates of R_{200} and M_{200} for the core of protoclusters at $z \sim 2.5$. Thus, at such overdense structures as in our case, it should be worthwhile to do this diagnostic which could provide interesting findings about our system.

The x component of the diagram is the projected distance from the cluster centre (RA, Dec.) = (12:36:55.92, +62:13:26.40), normalized in unit of R_{200}. The y component is the velocity offset from the systematic velocity of the protocluster along the *los*, normalized by the velocity dispersion of the protocluster. In particular, we use

$$R_{\rm proj} = \sqrt{(x_i - x_{\rm cl})^2 + (y_i - y_{\rm cl})^2}, \tag{6}$$

Downloaded from https://academic.oup.com/mnras/article/502/3/4558/6064312 by guest on 12 February 2026

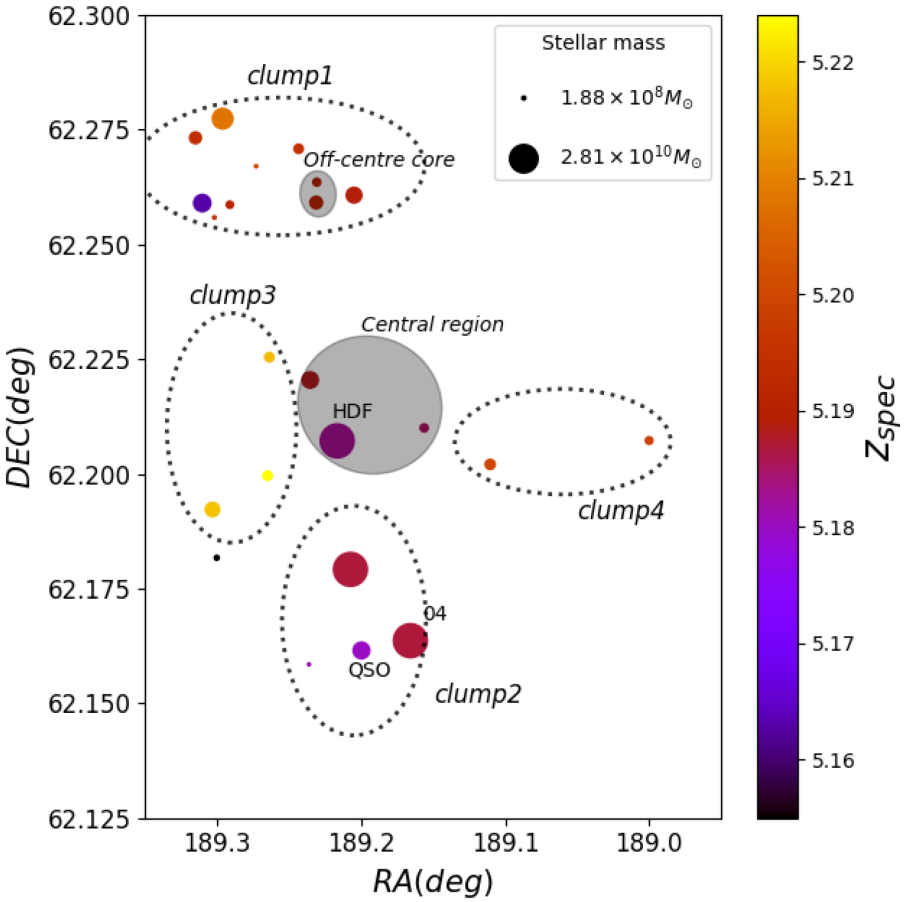


Figure 10. Position of the 23 sources used in the FoF analysis in right ascension and declination in degree. The sizes of the circles are in correspondence of different stellar masses (for the SMG and the galaxies #4 we considered the highest value of $M\star$), while the colour bar indicate the spectroscopic redshift. The dotted black ellipses enclose LAEs/LBGs in the NE clump1, south central clump2, SE clump3, and SW clump4. The shaded grey areas indicate the pair-like system in the NE region and the central region of the overdensity around the SMG.

$$\frac{\Delta v_i}{\sigma_{\rm cl}} = \frac{c(z_i - z_{\rm cl})}{(1+z_{\rm cl})\sigma_{\rm cl}}, \tag{7}$$

where (x, y, z) are the two spatial components and the component in redshift space and c is the speed of light. The blue solid lines correspond to the escape velocity of the cluster assuming a Navarro et al. (1996) halo density profile. We follow Rhee et al. (2017) and we calculate

$$v_{\rm esc} = \sqrt{\frac{2GM_{200}}{R_{200}} K(s)}, \tag{8}$$

where

$$K(s) = \frac{\ln(1+Cs)}{s} g(C), \tag{9}$$

$$s = \frac{r_{\rm 3D}}{R_{200}}, \tag{10}$$

$$g(C) = \left[\ln(1+C) - \frac{C}{1+C}\right]^{-1}, \tag{11}$$

C is the concentration parameter, fixed at $C = 6$ which is a typical value for cluster mass NFW haloes (Gill et al. 2004). The area within the dashed lines represents the area under the influence of the protocluster potential. In determining the velocity dispersion to compute R_{200} and M_{200} in equation (7) we assume that only the 18 galaxies in the central bin $5.18 \leq z \leq 5.208$ satisfy the NFW conditions. This choice ensures a clean sample with tight redshift distribution ($\Delta z = 0.028$) and enables us to not overestimate the velocity dispersion getting a broader distribution of objects in redshift space. Thus, following the method of Beers et al. (1990) and excluding the galaxies at the edges of protocluster (in the lower and higher redshift bin), we find that the velocity dispersion of the 18 sources is $\sigma_{\rm cl} = 1260\,{\rm km\,s^{-1}}$. We also separate the galaxies, according to their stellar mass. We separate the galaxies in two groups. The 'red' group with $M_\star \geq 2.0 \times 10^9\,{\rm M}_\odot$ and the 'blue' one with $M_\star < 2.0 \times 10^9\,{\rm M}_\odot$. Considering the schematic view of the orbit of a galaxy in phase-space diagram, we can distinguish several regions according to Jaffé et al. (2015). The SMG lies at a small projected protocluster centric radii ($R_{\rm proj}/R_{200} \sim 1$) and has a velocity that is remarkably similar to the systemic velocity of the protocluster ($\Delta v/\sigma \sim 0$), indicating that it might be settling into the BCG of the future $z = 0$ cluster. A group of 'red' galaxies is close to the central region ($R_{\rm proj}/R_{200} < 2$) and have small velocities. They are approaching the virialized region from the right-hand side. At $R_{\rm proj}/R_{200} > 2$ there is a number of 'blue' galaxies that are likely in groups in the outskirts of protocluster, infalling in the main structure. We also show in the phase-space diagram the position of galaxies at the edge of the redshift distribution which we excluded in the $v_{\rm esc}$ calculation. They have velocities close to the $v_{\rm esc}$ and within the region enclosed by these two curves. It is

Downloaded from https://academic.oup.com/mnras/article/502/3/4558/6064312 by guest on 12 February 2026

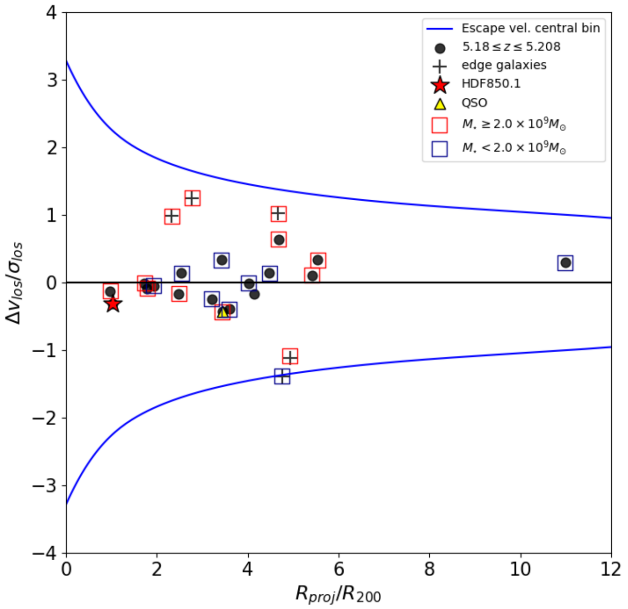


Figure 11. The observed phase-space diagram for the spectroscopically confirmed member galaxies in PCl-HDF850.1. The black circles are the 18 galaxies in the central bin $5.18 \leq z \leq 5.208$. The black crosses are the galaxies in the lower and higher redshift bin (the edges of protocluster). The red star refers to the SMG HDF750.1. The yellow triangle refers to the QSO. The red and blue squares around galaxies refers to galaxies with stellar masses $\geq 2.0 \times 10^9$ and $< 2.0 \times 10^9$ $M_\odot$, respectively. The solid blue lines correspond to the escape velocity in an NFW halo for the central bin. The solid horizontal line at $\Delta v/\sigma = 0$ corresponds to the systemic velocity of the protocluster.

very likely that they will remain bound by the massive halo of dark matter.

6 OVERDENSITY MASS CALCULATIONS

In our analysis we have paid particular attention to the complex multicomponent system in formation at $z = 5.2$. In order to put this protocluster into an evolutionary context and to compare it with other known high-z protoclusters and with the cosmological simulations, the goal of this section is to explore the halo mass of the whole structure and the descendant mass at $z = 0$.

6.1 Halo mass

We derive the halo mass at $z = 5.2$ with three different methods following Long et al. (2020). First of all, we estimate the total halo mass of protocluster by summing the individual halo associated with each galaxy and by using the stellar-to-halo abundance matching relationship presented in Behroozi, Wechsler & Conroy (2013). This method implicitly assumes galaxies as self-bound entities close to virialization. We excluded the galaxies #8 and #4 as we do not have any estimate of their stellar masses. We estimate the $M_{\rm DMH}$ ranging from 4.17×10^{10} to 3.49×10^{12} $M_\odot$ leading to a total halo mass of $M_{1,\rm tot} = 7.95 \times 10^{12}$ $M_\odot$. The second method consists in identifying the central galaxy and using its stellar mass. As we do not know the stellar mass of the #8, which corresponds to the SMG, we consider the most massive galaxy of our sample. Interpolating this value over the 'Behroozi relationship' we find $M_{2,\rm tot} = 1.9 \times 10^{12}$ $M_\odot$. Finally, in the last approach we sum up all masses of the individual cluster members to the total stellar mass of this system. We assume a fraction of 5 per cent of the baryonic to dark matter halo mass (Behroozi & Silk 2018). Thus, we estimate a halo mass of $M_{3,\rm tot} = 2.0 \times 10^{12}$ $M_\odot$. Assuming a halo mass of $M_{\rm tot} \approx 2{-}8 \times 10^{12}$ $M_\odot$ already in place at redshift $z = 5.2$, and simulated evolutionary tracks of protostructures from Chiang, Overzier & Gebhardt (2013) shown in fig. 7 in Long et al. (2020), the descendent mass in the local Universe is expected to be similar to a Virgo/Coma-like cluster. However, we do not include in the calculation the SMG (#8) and an LAE (#4). As a consequence, the corresponding halo mass has to be considered as a lower limit.

6.2 Present-day mass

The method we use for computing the present-day mass $M_{z=0}$ of this overdensity assumes a spherical collapse model (Steidel et al. 1998) where everything within the volume will collapse into a cluster. We first define the density contrast of our rest-frame UV bright sources (from now on UVgal) such as our LAEs and LBGs as

$$\delta_{\rm gal} = \frac{n_{\rm UVgal} - \bar{n}_{\rm UVgal}}{\bar{n}_{\rm UVgal}}, \tag{12}$$

where $n_{\rm UVgal}$ is the number density of rest-frame UV bright sources within the region under consideration and $\bar{n}_{\rm UVgal}$ is the mean number density of rest-frame UV bright sources in the field. We obtain the number densities of this source population by simply dividing the observed number counts of these sources in a given area. The spectroscopic sample for this analysis includes the sample of sources discovered by Walter et al. (2012). However, we will only consider the objects within the OSIRIS FoV. We find that 22 galaxies lie within the FoV area of 45 arcmin^2 (17×14 cMpc^2). The number density is $n_{\rm UVgal} = 0.49 \pm 0.10$ arcmin^{-2}. The uncertainty for the density measurement is calculated assuming the Poissonian noise $\sigma_N = \frac{\sqrt{N}}{\rm area}$, where N is the number of galaxies. We use as field number density the density published by Bouwens et al. (2015). At $z \sim 5$, the $\bar{n}_{\rm LAEs} = 0.2771 \pm 0.0194$ arcmin^{-2}. With these values, we find the number density contrast $\delta_{\rm gal} = 0.77 \pm 0.27$. The 2D density contrasts between protoclusters and the field are relatively small at high redshift. Because the number density by Bouwens et al. (2015) is calculated for a data set of bright UV LBG galaxies, the estimated $\delta_{\rm gal}$ has to be considered as an upper limit. To compute the mass of the overdensity contained in the volume occupied by the overdensity, we use the classical equation presented by Steidel et al. (1998)

$$M_{z=0} = \langle\rho\rangle V_{\rm true}(1 + \delta_{\rm m}), \tag{13}$$

where $\langle\rho\rangle$ is the mean matter density of the Universe at $z = 5.2$, $V_{\rm true} = \frac{V_{\rm obs}}{C}$ is the distortion corrected comoving observed volume and $\delta_{\rm m}$ is the matter density contrast. The value of $\delta_{\rm m}$ is expressed by the equation

$$1 + b\delta_{\rm m} = C(1 + \delta_{\rm gal}), \tag{14}$$

,where b is the bias parameter and C the correction factor for the redshift space distortion (Kaiser 1987; Steidel et al. 1998; Overzier 2016). Applying a linear interpolation to the relation found by Ouchi et al. (2018), we compute the bias parameter at redshift $z = 5.2$ to be $b = 3.45$. The matter density contrast $\delta_{\rm m}$ is interconnected to the C factor by the equation

$$C = 1 + f - f(1 + \delta_{\rm m})^{\frac{1}{3}}, \tag{15}$$

where f is a function of redshift and depends on the cosmological model (Steidel et al. 1998; Linder 2005)

$$f(z) = \Omega_{\rm m}(z)^{0.6}, \tag{16}$$

Downloaded from https://academic.oup.com/mnras/article/502/3/4558/6064312 by guest on 12 February 2026

which we take to be $\simeq 0.99$ at $z = 5.2$. Solving simultaneously the equations (14) and (15) in $\delta_{\rm m}$ and C, we derive

$$C = 0.94, \qquad \delta_{\rm m} = 0.19. \tag{17}$$

To estimate the observed volume, we multiplied the spatial extent and the sky projected area. In the *los* dimension, the effective spatial extent is represented by the difference in the radial comoving distance between the two redshift boundaries covered (from $z = 5.155$ to 5.224). The range of $\Delta z = 0.069$ is a factor ∼2 smaller than the redshift range probed by the medium-band filter ($\Delta z = 0.132$). Setting the volume (in redshift space) containing the overdensity as ∼17 × 14 × 34.8 cMpc^3, the corrected survey volume $V_{\rm true}$ = 8,811 cMpc^3 and the mean matter density of the Universe at $z = 5.2$ $\langle\rho\rangle = 4.1 \times 10^{10}\,{\rm M}_\odot\,{\rm cMpc}^{-3}$, we compute a lower limit of the mass of the overdensity from equation (13) that is $M_{z=0} = 4.3 \times 10^{14}\,{\rm M}_\odot$. The mass falls in the range typical of a Virgo type cluster, i.e. 3–10 × 10^{14} M$_\odot$. We can compare our present-day mass estimate with the prediction of simulations for a protocluster in literature associated with the radio galaxy TN J0924−2201 at $z = 5.2$ (Venemans et al. 2004; Overzier et al. 2006). For a window of 7 × 7 arcmin^2 and $\Delta z \sim 0.07$, similar to our window of observation, and galaxies with SFR > 1 M$_\odot$ yr^{-1}, Chiang et al. (2013) determined $\delta_{\rm gal} \sim 1.5^{+1.6}_{-1.0}$. Tuning the simulation predictions to this particular observational configuration, the present-day mass for this protocluster would be $M_{2201,z=0} = 4$–$9 \times 10^{14}\,{\rm M}_\odot$, consistent with our result.

Basing on the assumption about the $\delta_{\rm gal}$, the value of $\delta_{\rm m}$ should be considered an upper limit. The typical value for a protocluster at $z = 5$ is ∼0.2−0.4 (Suwa, Habe & Yoshikawa 2006). Considering this value of $\delta_{\rm m} = 0.19$, in a spherical collapse model (Mo & White 1996), this is related to a linear matter enhancement of $\delta_{\rm L}(z = 0) = \delta_{\rm m}(z = 5.2) \times 5 \sim 0.95$ (where 5 is the linear growth factor from $z = 5.2$ to $z = 0$). This does not exceed the collapse threshold of $\delta_{\rm c} = 1.68$. Therefore, the protocluster is expected to not collapse and virialize as a whole by now ($z = 0$), suggesting that only the main protocluster progenitor grows into a Virgo-like cluster at the present day, while the clumps are going to evolve separately into independent haloes. However, we are possibly observing only a part of a more complex and much larger structure. Generally, the size of protoclusters are larger than the area covered by one OSIRIS MOS pointing (FoV). Sizes of such structures are estimates to be up to 30 arcmin to 1 deg at the sky (Muldrew et al. 2015; Casey 2016). In Section 7, we will discuss our results also in the light of theoretical predictions.

7 THE FATE OF THE PROTOCLUSTER

7.1 General remarks

One of the main challenges when protoclusters are revealed is to interpret the observations and place them into an evolutionary context that can predict their growth. The cosmic build-up starts in filaments, the Universe's backbone. This complex web of interconnected patterns shows a large variety of structures and substructures, of different scales and densities, at their intersections (Evrard et al. 2002). However, a serious prediction of the fate of such structures is not easy, considering that their evolutionary history is a continuous adaptation in response to all environmental changes they experience. As a consequence, the different parameters that characterize the cosmic history of a protocluster depends on many components (e.g. dark matter, intracluster gas, environment imprints). Theoretically, the member galaxies of high-redshift protoclusters occupy individual dark matter haloes at the epoch at which they are being observed but later they will merge into a common halo by $z = 0$. The puzzle we try to examine in this section is to understand whether the future fate of galaxies within a newly confirmed overdensity at $z \sim 5.2$ will be in a single collapsed halo or the individual density peaks will evolve in independent haloes as part of a supercluster. It is important to point out that the results of the analysis we carried out, using our spectroscopic observations and literature data (Walter et al. 2012), do not cover the full area of the overdensity as traced by the parent candidate member sample of 55 LAEs and LGBs found by Arrabal Haro et al. (2018). We note that the SHARDS region in GOODS-N has a size of about 130 arcmin^2 (Pérez-González et al. 2013). However, although we cannot establish the spatial extent of the protocluster and a definitive evolutionary framework, we try to address this question by examining the key clues we found.

7.2 A collapsed system or a supercluster with filament bridges?

As stated in the previous sections, we find a very extended protocluster, 34.8 cMpc (∼5.6 Mpc physical size) with an elongated shape from NE to SW, formed by multiple components linked through filaments clearly shown in the redshift distribution. Sizes of high-redshift protoclusters (as progenitors of local galaxy clusters) have been widely studied by using especially numerical simulations, depending significantly on the resultant halo mass at $z = 0$. Suwa et al. (2006) at $z = 4$−5 found that the progenitors are extended regions of typically 20–40 cMpc with dark matter haloes in excess of $10^{12}h^{-1}\,{\rm M}_\odot$. Chiang et al. (2013) defined an effective radius $R_{\rm e}$ which enclose 40 per cent of the total mass of a protocluster, estimating that the typical diameter $2R_{\rm e}$ of a protocluster at $z \sim 5$ is of $2R_{\rm e} = 13.2^{+2.8}_{-2.4}$ cMpc and $2R_{\rm e} = 18.8^{+3.2}_{-3.2}$ cMpc for progenitors of Virgo-type clusters [(3–10) × 10^{14} M$_\odot$] and Coma-type clusters (> 10^{15} M$_\odot$), respectively. Using a different measure of the protocluster radius Muldrew et al. (2015) found that the average radius that encloses 90 per cent of the stellar mass of a protocluster at $z \sim 5$ is ∼2−3(4) Mpc in physical scale for final cluster masses of (1 − 9) × 10^{14} M$_\odot$(> 10^{15} M$_\odot$). We identify in our protocluster four substructures around the central region which hosts the SMG. The NE region contains an off-centre core, whose galaxies are members of a pair-like system with a dynamical mass $M_{200} \sim 9.4 \times 10^{12}\,{\rm M}_\odot$. From the clustering analysis, we identify this region as the most evolved region. This might be evidence of a 'proto-red sequence' in formation. The presence of a pair-like subgroup is statistically reliable in protoclusters, because they form faster in the core in agreement with the hierarchical structure formation model (Toshikawa et al. 2014, Toshikawa et al. 2016). Kubo et al. (2015) predict that such rare groups hosted in massive haloes with $M_{\rm vir} = 10^{13.4}$–$10^{14.0}\,{\rm M}_\odot$ might evolve and merge into the BCGs of the most massive clusters at present. The other three components identified in our structure, whose galaxies do not span the same physical volume as the galaxies in the NE region, are an indication of the young evolutionary state of this overdensity at $z = 5.2$ around the dusty starburst HDF850.1.

Similar large complex structures are rare in the distant Universe, but not unexpected (see e.g. Muldrew et al. 2015; Casey 2016). For example, Dey et al. (2016) found two overdense regions at $z = 3.786$, the protocluster PC 17.96+32.3 through Keck/DEIMOS observations. The small velocity dispersions of its subgroups and the spatial distribution suggest that these systems are dynamically young and in the process of merging. Topping et al. (2016, 2018) investigated the nature and evolution of large-scale structures within the SSA22 protocluster region at $z = 3.09$ using both KECK/LIRS spectroscopic

Downloaded from https://academic.oup.com/mnras/article/502/3/4558/6064312 by guest on 12 February 2026

observations and simulations. They found that the observed double-peaked structure in the SSA22 redshift distribution corresponds not to a single coalescing cluster but rather to two different cluster progenitors with masses of $\sim 10^{15}$ and $> 10^{14}\,h^{-1}\,\mathrm{M}_{\odot}$. Recently, Toshikawa et al. (2020) carried out optical follow-up spectroscopy on three overdense regions at $z = 4.898$, 3.721, and 3.834 in the CFHTLS Deep Fields. They found that small groups in large assembly structures appear already at $z \sim 4-5$ in parallel with the formation of the protocluster core. However, their evolution depends on the halo mass. Indeed, according to theoretical predictions, if the subgroups have quite a small redshift separation from the main protocluster component, and the protocluster is the progenitor of a significantly rich cluster ($> 10^{15}\,\mathrm{M}_{\odot}$) at $z = 0$, it is likely possible that the neighbouring groups will be incorporated into a single halo by $z = 0$. Alternatively, the subgroups will evolve in satellites of a supercluster by $z = 0$. A massive multicomponent supercluster called the 'Hyperion' has been unveiled by Cucciati et al. (2018) at $z \sim 2.45$ in the COSMOS field using the spectroscopic VUDS, complemented by the zCOSMOS-Deep spectroscopic sample. They found a complex structure which contains at least seven density peaks with masses in the range $\sim 0.1 \times 10^{14}$–$2.7 \times 10^{14}\,\mathrm{M}_{\odot}$ that are independently evolving and in process of collapsing. Several of these density peaks have been previously reported by e.g. Diener et al. (2013), Casey et al. (2015), and Wang et al. (2016).

In the light of the above considerations and the detailed characterization of this overdensity, we can speculate about the fate of our massive protocluster at $z = 5.2$. From the analysis of the velocity structure and spatial distribution of all components of this protocluster, we demonstrated the existence of a large-scale structure around the SMG HDF850.1. The spatial extent and the complex structure show that it is very extended in several directions. The neighbouring clumps which belong to the edges of the structure and are connected to the highest overdense region through rope-like filaments, have small separations from the central core of this protocluster around the well-known SMG ($\Delta z < 0.04$). According to simulations (Chiang et al. 2013) and other known high-redshift galaxy protoclusters (Toshikawa et al. 2020), we can assess that the main progenitor of this structure is bound to collapse into a Virgo-like galaxy cluster at $z = 0$ with neighbouring independent evolving clumps, comparable with rather elongated filaments typical of superclusters. However, our results are derived from a pilot spectroscopic program of a structure that could be incomplete in terms of areal coverage of the field. Additionally, all the mass estimates we performed are conservative estimates. Thus, we expect that a more complete census of the galaxies residing in the protocluster and its surroundings can reveal an evolution at $z = 0$ similar to a more massive Coma-like cluster ($> 10^{15}\,\mathrm{M}_{\odot}$), which eventually incorporate the neighbouring clumps into a single halo. Such a massive structure is not surprising at $z > 5$ since we already have evidence of massive protoclusters at this epoch. Capak et al. (2011) found at $z = 5.3$ a cluster of massive galaxies which extends over >13 Mpc, and contains a luminous quasar as well as a system rich in molecular gas. At earlier epochs, Jiang et al. (2018) found at $z = 5.7$ a protocluster with at least 41 confirmed members. It occupies a volume of about $35 \times 35 \times 35$ cubic comoving Mpc and is predicted to collapse into a galaxy Coma-like cluster with a mass of $3.6 \pm 0.9 \times 10^{15}\,\mathrm{M}_{\odot}$. In our pilot spectroscopical observations, we find strong evidence that this is one of the richest protoclusters beyond redshift $z = 5$.

8 CONCLUSIONS

We conducted a pilot spectroscopic follow-up with the multi-object spectrograph OSIRIS on the GTC of a sample of 17 rest-frame UV sources (LAEs and LGBs) selected from AH18. These sources are candidate members of the protocluster PCL−HDF850.1 at $z = 5.2$. The major aim is to probe the existence of one of the largest known and most overdense high-redshift structure beyond redshift $z = 5$. The main results of this work are summarized below:

(i) We spectroscopically confirmed 13 cluster members, 10 LAEs and 3 LBGs, that are part of an already known overdensity found by Walter et al. (2012) at redshift $z = 5.2$. The objects span a redshift range between $5.155 \leq z_{\mathrm{gal}} \leq 5.224$. 3 of them match the 13 sources discovered by Walter et al. (2012) while 10 members are completely new.

(ii) We investigate the properties of 13 members and we obtained spectra for them. The analysis of the Lyα equivalent widths and SFRs are consistent with starburst galaxies. Among the candidates we detect a powerful AGN, the quasar CXOHDFNJ123647.9+620941 (already spectroscopically identified in the Chandra Deep Field-North by Barger et al. 2002, 2003). Except for the AGN, we cannot find any significant differences among the properties of these galaxies.

(iii) The dusty starburst HDF850.1 seems to evolve into the BCG of this cluster in formation. Interestingly, none of the confirmed members (beside the SMG) are bright in the far-infrared/sub-mm/radio wavelength regime. The SFR of this structure seems to be dominated by the well-known dusty starburst.

(iv) We apply the FoF analysis on the 13 confirmed LAEs and LBGs at $z = 5.2$ from this work, combined with the sample of 10 members from Walter et al. (2012) in order to assess the possibility of bounded regions. All 23 sources span a comoving distance of 34.8 cMpc (diameter). From the histogram of the redshift distribution and the clustering analysis we find a clear segregation of galaxies along the structure of the protocluster. In the NE part we find a region with ten galaxies, nine in a narrow redshift range between $5.183 \leq z \leq 5.208$ and one at $z = 5.163$. We define this region as clump1 with an 'off-centre core'. It could also represent the 'proto-red sequence' of this overdensity. In the southern part of this structure, we find three additional clumps with $\Delta z < 0.04$, which surround the central core with the SMG HDF850.1. They could evolve independently from the main protocluster.

(v) Most probably, our spectroscopic observation (one OSIRIS pointing) do not cover the full area of the overdensity. We put this protocluster into an evolutionary framework and predict its fate comparing our results with other known high-z protoclusters and with simulations. We find that the size of the protocluster and the estimate of the mass using the spherical collapse model are consistent with simulations and suggest that this structure does not collapse as a whole but the main progenitor will evolve into a cluster of mass $\sim 4.3 \times 10^{14}\,\mathrm{M}_{\odot}$ by $z = 0$ similar to a Virgo-cluster, with independent satellite haloes which will possibly be incorporated in a single halo if a more detailed analysis of this impressive structure indicates that the protocluster is the progenitor of a more massive Coma-like cluster ($> 10^{15}\,\mathrm{M}_{\odot}$).

Based on the results of this pilot program, we prove the existence of a rich overdensity at $z = 5.2$. Considering that in AH18 we have photometrically identified a total of 44 potential new members of this overdensity, with this program we observed less than 50 per cent of this impressive large structure. Thus, future GTC OSIRIS observations will aim to fully characterize this rich protocluster with all potential members.

Downloaded from https://academic.oup.com/mnras/article/502/3/4558/6064312 by guest on 12 February 2026

ACKNOWLEDGEMENTS

We thank the referee for his/her useful comments, which allowed us to clarify some parts of the paper. HD acknowledges financial support from the Spanish Ministry of Science, Innovation and Universities (MICIU) under the 2014 Ramón y Cajal program RYC-2014-15686. HD and JMRE acknowledge financial support from the Spanish Ministry of Science, Innovation and Universities (MICIU) under the AYA2017-84061-P, co-financed by FEDER (European Regional Development Funds), and from the Agencia Estatal de Investigación del Ministerio de Ciencia e Innovación (AEI-MCINN) under grant (La evolución de los cúmulos de galaxias desde el amanecer hasta el mediodía cósmico) with reference (PID2019-105776GB-I00/ DOI:10.13039/501100011033). RC, PAH, JMRE, and CMT want to acknowledge support from the Spanish Ministry Science, Innovation and Universities (MICIU) under grants AYA2015-70498-C2-1-R, AYA2013-47742-C4-2-P, and AYA2016-79724-C4-2-P. PGPG acknowledges support from Spanish Government grant PGC2018-093499-B-I00. This study is based on observations made with the Gran Telescopio Canarias (GTC), installed in the Spanish Observatorio del Roque de los Muchachos of the Instituto de Astrofísica de Canarias, in the island of La Palma. We would like to thank Emanuele Daddi, José Eduardo Méndez Delgado, Daizhong Liu, Arianna Long, Roderik Obverzier, José Pérez Martínez, and Andrea Negri for valuable help to specific issues of this manuscript.

DATA AVAILABILITY

The raw data underlying this article are available in the GTC public archive at https://gtc.sdc.cab.inta-csic.es/gtc/ and can be accessed with the proposal number GTC122-17B. The reduced data underlying this article will be shared on reasonable request to the corresponding author.

REFERENCES

Adams S. M., Martini P., Croxall K. V., Overzier R. A., Silverman J. D., 2015, MNRAS, 448, 1335
Andreon S., Willis J., Quintana H., Valtchanov I., Pierre M., Pacaud F., 2004, MNRAS, 353, 353
Andreon S., Maughan B., Trinchieri G., Kurk J., 2009, A&A, 507, 147
Arrabal Haro P. et al., 2018, MNRAS, 478, 3740
Arrabal Haro P. et al., 2020, MNRAS, 495, 1807
Bahcall N. A., Ostriker J. P., Perlmutter S., Steinhardt P. J., 1999, Science, 284, 1481
Baldry I. K., Balogh M. L., Bower R. G., Glazebrook K., Nichol R. C., Bamford S. P., Budavari T., 2006, MNRAS, 373, 469
Balogh M. L. et al., 2011, MNRAS, 412, 2303
Barger A. J., Cowie L. L., Brandt W. N., Capak P., Garmire G. P., Hornschemeier A. E., Steffen A. T., Wehner E. H., 2002, AJ, 124, 1839
Barger A. J., Cowie L. L., Capak P., Alexand er D. M., Bauer F. E., Brandt W. N., Garmire G. P., Hornschemeier A. E., 2003, ApJ, 584, L61
Beers T. C., Flynn K., Gebhardt K., 1990, AJ, 100, 32
Behroozi P., Silk J., 2018, MNRAS, 477, 5382
Behroozi P. S., Wechsler R. H., Conroy C., 2013, ApJ, 770, 57
Berlind A. A. et al., 2006, ApJS, 167, 1
Boquien M., Burgarella D., Roehlly Y., Buat V., Ciesla L., Corre D., Inoue A. K., Salas H., 2019, A&A, 622, A103
Bouwens R. J. et al., 2015, ApJ, 803, 34
Brocklehurst M., 1971, MNRAS, 153, 471
Burgarella D., Buat V., Iglesias-Páramo J., 2005, MNRAS, 360, 1413
Cai Z. et al., 2016, ApJ, 833, 135
Calvi R. et al., 2019, MNRAS, 489, 3294
Capak P. L. et al., 2011, Nature, 470, 233
Casey C. M., 2016, ApJ, 824, 36
Casey C. M. et al., 2015, ApJ, 808, L33
Castellano M. et al., 2018, ApJ, 863, L3
Cepa J., 2010, Astrophysics and Space Science Proceedings, Vol. 14, OSIRIS: Final Characterization and Scientific Capabilities. Springer-Verlag, Berlin, Heidelberg, p. 15
Chanchaiworawit K. et al., 2019, ApJ, 877, 51
Charlot S., Fall S. M., 1993, ApJ, 415, 580
Chiang Y.-K., Overzier R., Gebhardt K., 2013, ApJ, 779, 127
Chiang Y.-K., Overzier R. A., Gebhardt K., Henriques B., 2017, ApJ, 844, L23
Clements D. L. et al., 2014, MNRAS, 439, 1193
Clements D. L. et al., 2016, MNRAS, 461, 1719
Cochrane R. K., Best P. N., Sobral D., Smail I., Geach J. E., Stott J. P., Wake D. A., 2018, MNRAS, 475, 3730
Contini E., De Lucia G., Hatch N., Borgani S., Kang X., 2016, MNRAS, 456, 1924
Cooke E. A., Hatch N. A., Muldrew S. I., Rigby E. E., Kurk J. D., 2014, MNRAS, 440, 3262
Cucciati O. et al., 2014, A&A, 570, A16
Cucciati O. et al., 2018, A&A, 619, A49
Daddi E. et al., 2009, ApJ, 694, 1517
Daddi E. et al., 2017, ApJ, 846, L31
Dannerbauer H. et al., 2014, A&A, 570, A55
Davis A. J., Natarajan P., 2010, MNRAS, 407, 691
Davis M., Efstathiou G., Frenk C. S., White S. D. M., 1985, ApJ, 292, 371
Davis A. J., D'Aloisio A., Natarajan P., 2011, MNRAS, 416, 242
De Lucia G., Blaizot J., 2007, MNRAS, 375, 2
Dey A., Lee K.-S., Reddy N., Cooper M., Inami H., Hong S., Gonzalez A. H., Jannuzi B. T., 2016, ApJ, 823, 11
Dickinson M., Papovich C., Ferguson H. C., Budavári T., 2003, ApJ, 587, 25
Diener C. et al., 2013, ApJ, 765, 109
Djorgovski S. G., Stern D., Mahabal A. A., Brunner R., 2003, ApJ, 596, 67
Dopita M. A., Sutherland R. S., 2003, Astrophysics of the Diffuse Universe, Astronomy and astrophysics library, Springer, Berlin, New York
Dunlop J. S. et al., 2004, MNRAS, 350, 769
Einasto J., Klypin A. A., Saar E., Shandarin S. F., 1984, MNRAS, 206, 529
Eke V. R. et al., 2004, MNRAS, 355, 769
Evrard A. E. et al., 2002, ApJ, 573, 7
Falder J. T. et al., 2011, ApJ, 735, 123
Gavazzi R., Soucail G., 2007, A&A, 462, 459
Gill S. P. D., Knebe A., Gibson B. K., Dopita M. A., 2004, MNRAS, 351, 410
Gladders M. D., Yee H. K. C., 2005, ApJS, 157, 1
Gobat R. et al., 2011, A&A, 526, A133
Goto T. et al., 2008, PASJ, 60, S531
Gottlöber S., Yepes G., 2007, ApJ, 664, 117
Greenslade J. et al., 2019, MNRAS, 490, 5317
Gunn J. E., 1977, ApJ, 218, 592
Gunn J. E., Gott J., Richard I., 1972, ApJ, 176, 1
Haines C. P. et al., 2015, ApJ, 806, 101
Harikane Y. et al., 2019, ApJ, 883, 142
Hashimoto T. et al., 2015, ApJ, 812, 157
Hashimoto T. et al., 2019, PASJ, 71, 71
Hatch N. A. et al., 2011a, MNRAS, 410, 1537
Hatch N. A., Kurk J. D., Pentericci L., Venemans B. P., Kuiper E., Miley G. K., Röttgering H. J. A., 2011b, MNRAS, 415, 2993
Hayashi M., Kodama T., Tadaki K.-i., Koyama Y., Tanaka I., 2012, ApJ, 757, 15
Hennawi J. F., Prochaska J. X., Cantalupo S., Arrigoni-Battaia F., 2015, Science, 348, 779
Hetznecker H., Burkert A., 2006, MNRAS, 370, 1905
Hopkins A. M., 2004, ApJ, 615, 209
Huchra J. P., Geller M. J., 1982, ApJ, 257, 423
Hughes D. H. et al., 1998, Nature, 394, 241
Hung C.-L. et al., 2016, ApJ, 826, 130
Husband K., Bremer M. N., Stanway E. R., Davies L. J. M., Lehnert M. D., Douglas L. S., 2013, MNRAS, 432, 2869
Ivison R. J. et al., 2013, ApJ, 772, 137
Jaffé Y. L., Smith R., Candlish G. N., Poggianti B. M., Sheen Y.-K., Verheijen M. A. W., 2015, MNRAS, 448, 1715

Downloaded from https://academic.oup.com/mnras/article/502/3/4558/6064312 by guest on 12 February 2026

Jang-Condell H., Hernquist L., 2001, ApJ, 548, 68
Jeffrey N. et al., 2018, MNRAS, 479, 2871
Jenkins A., Frenk C. S., White S. D. M., Colberg J. M., Cole S., Evrard A. E., Couchman H. M. P., Yoshida N., 2001, MNRAS, 321, 372
Jiang L. et al., 2018, Nat. Astron., 2, 962
Kaiser N., 1987, MNRAS, 227, 1
Kajisawa M., Kodama T., Tanaka I., Yamada T., Bower R., 2006, MNRAS, 371, 577
Kashikawa N., Kitayama T., Doi M., Misawa T., Komiyama Y., Ota K., 2007, ApJ, 663, 765
Kato Y. et al., 2016, MNRAS, 460, 3861
Kauffmann G., White S. D. M., Heckman T. M., Ménard B., Brinchmann J., Charlot S., Tremonti C., Brinkmann J., 2004, MNRAS, 353, 713
Kennicutt, Robert C. J., 1998, ApJ, 498, 541
Kodama T., Tanaka I., Kajisawa M., Kurk J., Venemans B., De Breuck C., Vernet J., Lidman C., 2007, MNRAS, 377, 1717
Kravtsov A. V., Borgani S., 2012, ARA&A, 50, 353
Kubo M., Yamada T., Ichikawa T., Kajisawa M., Matsuda Y., Tanaka I., 2015, ApJ, 799, 38
Kuiper E. et al., 2011, MNRAS, 417, 1088
Kurk J. D. et al., 2000, A&A, 358, L1
Kurk J. D., Pentericci L., Röttgering H. J. A., Miley G. K., 2004a, A&A, 428, 793
Kurk J. D., Pentericci L., Overzier R. A., Röttgering H. J. A., Miley G. K., 2004b, A&A, 428, 817
Lacaille K. M. et al., 2019, MNRAS, 488, 1790
Lacey C., Cole S., 1994, MNRAS, 271, 676
Laporte N. et al., 2015, ApJ, 810, 130
Le Fevre O., Deltorn J. M., Crampton D., Dickinson M., 1996, ApJ, 471, L11
Lemaux B. C. et al., 2014, A&A, 572, A41
Lewis A. J. R. et al., 2018, ApJ, 862, 96
Linder E. V., 2005, Phys. Rev. D, 72, 043529
Liu D. et al., 2018, ApJ, 853, 172
Long A. S. et al., 2020, ApJ, 898, 133
Madau P., Dickinson M., 2014, ARA&A, 52, 415
Mantz A. B. et al., 2014, ApJ, 794, 157
Matsuda Y. et al., 2011, MNRAS, 416, 2041
Miley G. K. et al., 2004, Nature, 427, 47
Miller T. B. et al., 2018, Nature, 556, 469
Miller J. S. A., Bolton J. S., Hatch N., 2019, MNRAS, 489, 5381
Mo H. J., White S. D. M., 1996, MNRAS, 282, 347
Morselli L. et al., 2014, A&A, 568, A1
Muldrew S. I., Hatch N. A., Cooke E. A., 2015, MNRAS, 452, 2528
Muldrew S. I., Hatch N. A., Cooke E. A., 2018, MNRAS, 473, 2335
Mullis C. R., Rosati P., Lamer G., Böhringer H., Schwope A., Schuecker P., Fassbender R., 2005, ApJ, 623, L85
Muzzin A. et al., 2009, ApJ, 698, 1934
Navarro J. F., Frenk C. S., White S. D. M., 1996, ApJ, 462, 563
Navarro J. F., Frenk C. S., White S. D. M., 1997, ApJ, 490, 493
Neri R., Downes D., Cox P., Walter F., 2014, A&A, 562, A35
Noll S., Burgarella D., Giovannoli E., Buat V., Marcillac D., Muñoz-Mateos J. C., 2009, A&A, 507, 1793
Oke J. B., 1990, AJ, 99, 1621
Oke J. B., Gunn J. E., 1983, ApJ, 266, 713
Oman K. A., Hudson M. J., Behroozi P. S., 2013, MNRAS, 431, 2307
Oteo I. et al., 2018, ApJ, 856, 72
Otí-Floranes H., Mas-Hesse J. M., 2010, A&A, 511, A61
Ouchi M. et al., 2005, ApJ, 620, L1
Ouchi M. et al., 2009, ApJ, 706, 1136
Ouchi M. et al., 2018, PASJ, 70, S13
Overzier R. A., 2016, A&AR, 24, 14
Overzier R. A. et al., 2006, ApJ, 637, 58
Overzier R. A., Guo Q., Kauffmann G., De Lucia G., Bouwens R., Lemson G., 2009, MNRAS, 394, 577
Owen F. N., 2018, ApJS, 235, 34
Pascarelle S. M., Windhorst R. A., Driver S. P., Ostrand er E. J., Keel W. C., 1996, ApJ, 456, L21
Pavesi R. et al., 2018, ApJ, 861, 43
Peebles P. J. E., White S. D. M., 1981, Phys. Today, 34, 62
Pentericci L. et al., 2000, A&A, 361, L25
Pérez-González P. G. et al., 2013, ApJ, 762, 46
Planck Collaboration XXVII, 2015, A&A, 582, A30
Ragone-Figueroa C., Granato G. L., Ferraro M. E., Murante G., Biffi V., Borgani S., Planelles S., Rasia E., 2018, MNRAS, 479, 1125
Rhee J., Smith R., Choi H., Yi S. K., Jaffé Y., Candlish G., Sánchez-Jánssen R., 2017, ApJ, 843, 128
Riechers D. A. et al., 2010, ApJ, 720, L131
Riechers D. A. et al., 2013, Nature, 496, 329
Riechers D. A. et al., 2014, ApJ, 796, 84
Riechers D. A. et al., 2020, ApJ, 895, 81
Rodríguez Espinosa J. M. et al., 2020, MNRAS, 495, L17
Rosati P., Borgani S., Norman C., 2002, ARA&A, 40, 539
Rosati P. et al., 2004, AJ, 127, 230
Shan H. et al., 2012, ApJ, 748, 56
Shapley A. E., Steidel C. C., Pettini M., Adelberger K. L., 2003, ApJ, 588, 65
Shimakawa R., Kodama T., Tadaki K. I., Tanaka I., Hayashi M., Koyama Y., 2014, MNRAS, 441, L1
Sobral D., Smail I., Best P. N., Geach J. E., Matsuda Y., Stott J. P., Cirasuolo M., Kurk J., 2013, MNRAS, 428, 1128
Stanford S. A. et al., 2006, ApJ, 646, L13
Staniszewski Z. et al., 2009, ApJ, 701, 32
Steidel C. C., Adelberger K. L., Dickinson M., Giavalisco M., Pettini M., Kellogg M., 1998,ApJ, 492, 428
Steidel C. C., Adelberger K. L., Shapley A. E., Pettini M., Dickinson M., Giavalisco M., 2000, ApJ, 532, 170
Steidel C. C., Adelberger K. L., Shapley A. E., Erb D. K., Reddy N. A., Pettini M., 2005, ApJ, 626, 44
Steidel C. C., Erb D. K., Shapley A. E., Pettini M., Reddy N., Bogosavljević M., Rudie G. C., Rakic O., 2010, ApJ, 717, 289
Stevens J. A., Jarvis M. J., Coppin K. E. K., Page M. J., Greve T. R., Carrera F. J., Ivison R. J., 2010, MNRAS, 405, 2623
Stiavelli M. et al., 2005, ApJ, 622, L1
Strazzullo V. et al., 2016, ApJ, 833, L20
Suwa T., Habe A., Yoshikawa K., 2006, ApJ, 646, L5
Tang M., Stark D. P., Chevallard J., Charlot S., 2019, MNRAS, 489, 2572
Tody D., 1986, in Crawford D. L., ed., Proc. SPIE Conf. Ser. Vol. 627, Instrumentation in Astronomy VI. SPIE, Bellingham, p. 733
Topping M. W., Shapley A. E., Steidel C. C., 2016, ApJ, 824, L11
Topping M. W., Shapley A. E., Steidel C. C., Naoz S., Primack J. R., 2018, ApJ, 852, 134
Toshikawa J. et al., 2014, ApJ, 792, 15
Toshikawa J. et al., 2016, ApJ, 826, 114
Toshikawa J. et al., 2018, PASJ, 70, S12
Toshikawa J., Malkan M. A., Kashikawa N., Overzier R., Uchiyama H., Ota K., Ishikawa S., Ito K., 2020, ApJ, 888, 89
Trainor R. F., Steidel C. C., 2012, ApJ, 752, 39
Venemans B. P. et al., 2004, A&A, 424, L17
Venemans B. P. et al., 2005, A&A, 431, 793
Venemans B. P. et al., 2007, A&A, 461, 823
Walter F. et al., 2012, Nature, 486, 233
Wang L., De Lucia G., Weinmann S. M., 2013, MNRAS, 431, 600
Wang T. et al., 2016, ApJ, 828, 56
Weinmann S. M., van den Bosch F. C., Yang X., Mo H. J., 2006, MNRAS, 366, 2
White M., 2001, A&A, 367, 27
Wilson G. et al., 2009, ApJ, 698, 1943
Wittman D., Dell'Antonio I. P., Hughes J. P., Margoniner V. E., Tyson J. A., Cohen J. G., Norman D., 2006, ApJ, 643, 128
Wold M., Armus L., Neugebauer G., Jarrett T. H., Lehnert M. D., 2003, AJ, 126, 1776
Zirm A. W. et al., 2008, ApJ, 680, 224

This paper has been typeset from a TEX/LATEX file prepared by the author.

Downloaded from https://academic.oup.com/mnras/article/502/3/4558/6064312 by guest on 12 February 2026